Nonlinear power-dependent effects in exchange-coupled magnetic bilayers

Aaron M. Ferona and Robert E. Camley
Center for Magnetism and Magnetic Nanostructures University of Colorado at Colorado Springs Colorado Springs, Colorado 80918, USA

(Received 6 August 2018; revised manuscript received 2 January 2019; published 5 February 2019)

We investigate the dynamics of exchange-coupled ferromagnetic films in the nonlinear limit and find a number of interesting features. The introduction of asymmetries in the magnetic driving field can produce a power-dependent localization of the magnetization oscillations, in one film or the other, by way of the optic mode frequency shifting in the large field limit. A nonlinear mixing of the acoustic and optic modes in the antiferromagnetically coupled system leads to quasiperiodic and multiperiodic composite modes. Numerical ferromagnetic resonance experiments will show additional absorption peaks (in the 20–50 GHz range) which have a rapid increase in strength with input power. The results are calculated through linearization techniques and numerical solutions of the Landau-Lifshitz-Gilbert equation. The nonlinear (and linear) behavior is illustrated through Poincaré section bifurcation diagrams.

DOI: 10.1103/PhysRevB.99.064405

I. INTRODUCTION

Our research is motivated, in part, by the quantum double-well problem. In the typical linear and nonlinear double-well problem the wells are symmetric with a finite barrier. Solutions of the symmetric system can be found via Wentzel-Kramers-Brillouin approximation or numerically and result in an even ground state wave function and odd first excited state wave function. The probability (modulus squared) that the particle is contained in either well is the same for the symmetric double-well problem. In contrast, when an amplitude dependent (nonlinear) potential is added to the Schrödinger equation, the symmetry is broken and one can localize a particle to be primarily contained in one well or the other [1,2].

The nonlinear double-well problem raises the question of whether a similar phenomenon could occur in a nonlinear magnetic bilayer system. If the phenomena can be observed in a magnetic bilayer system it may be possible to use the system as a power limiter or filter [3–5], where one film can absorb a large fraction of electromagnetic energy during a power spike but otherwise behave as intended under nominal conditions. For example, a novel nanoscale device would be of interest in military systems where much attention is focused on electronic systems performance under a variety of abnormal or hostile scenarios.

Magnetic thin-film structures have been a primary interest since the development of molecular beam epitaxy. The ability of material scientists to grow high quality magnetic layered samples has accelerated developments in nanoscale magnetic structures [6]. There are many possible magnetic structures and configurations [7–14], but in this paper we constrain our discussion to ferromagnetic (F) and antiferromagnetic (AF) resonances of two coupled magnetic layers separated by a nonmagnetic spacer. These systems have been studied in detail by many different authors [6,7,12,15,16], but the work presented here is primarily focused on magnetic bilayer behavior in the nonlinear regime, whereas much of the previous analyses focused on linear responses. Investigations of the nonlinear behavior have only recently begun. In particular, there are a series of papers [17–19] which investigate, both theoretically and experimentally, the nonlinear frequency shift of the eigenmodes for coupled films driven by spin currents, however they do not address localization, resonance absorption, or the possibility of new modes at different frequencies, the topics in the current paper.

The Landau-Lifshitz-Gilbert (LLG) equation is an inherently nonlinear equation describing magnetization dynamics. This has led researchers to investigate nonlinear magnetization phenomena in many different systems [20–32]. The analysis we present here on nonlinear effects in exchange-coupled bilayers has been guided by these previous researchers in the field of magnetization dynamics.

We find a number of interesting results in our study of nonlinear dynamics of exchange-coupled films:

(1) For ferromagnetic coupling the spin excitation can be localized in one film or the other by changing the input power level. As the input power is increased near the acoustic or optic mode frequency of the structure, the energy becomes localized in one of the films.

(2) The antiferromagnetically exchange-coupled system is found to have a strong tunable high-frequency (20–50 GHz) mode comprised of both the acoustic and optic mode frequencies. Resonance absorption measurements show that this mode has a critical driving field strength where there is a rapid onset of microwave absorption as the power is increased.

The acoustic modes of magnetic thin-film systems have received a lot of attention due to their large susceptibility compared with that of the optic mode [7], but the strong response of the acoustic mode generally only occurs at lower frequencies (1–10 GHz). Because the electronics industry is continually pushing for faster response times, this has led researchers to search for ways to increase the operational frequency of the acoustic mode. In contrast, we find that the acoustic mode can be coupled to the higher frequency optic mode to generate large susceptibilities at the acoustic

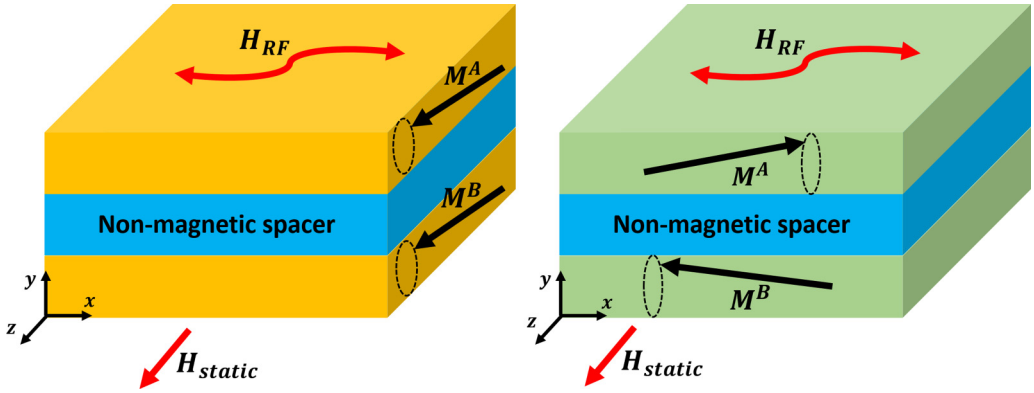

FIG. 1. Ferromagnetic (left) and antiferromagnetic (right) bilayer coupling configurations.

plus optic mode frequency. The strong resonance of this nonlinear composite mode is shown to occur under a variety of different magnetization configurations and is highly tunable by various control parameters. These modes may be of interest to researchers who are exploring microwave magnetic devices [12,33].

In Sec. II we present the magnetic bilayer configurations under investigation along with the equations of motion and numerical methods. Section III discusses two different linearization methods depending on the magnetic configuration, as well as the dispersion relations. In Sec. IV we show that magnetization oscillations of one of the exchange-coupled films can become localized under time-harmonic excitation of a microwave field. Sections V and VI explore a fascinating composite mode composed of both the acoustic and optic frequencies in the antiferromagnetic system. Finally, in Sec. VII we summarize our significant results and conclusions.

II. EQUATIONS OF MOTION AND NUMERICAL ANALYSIS

In the analysis presented here we use the macrospin approximation, where we have assumed the magnetization is uniform within each film. This approach is valid in the ultrathin film limit where the strong exchange forces hold the spins in adjacent atomic layers in line with one another [13]. The macrospin approach has been well established by researchers connecting experimental results with the theory [11,15,34] and allows a more analytic approach compared to micromagnetics [35].

The magnetic bilayer configurations considered in this paper are shown in Fig. 1. The macrospins $\boldsymbol{M}^A$ and $\boldsymbol{M}^B$ represent the magnetization in film A and film B, respectively. For ferromagnetic coupling (left side of Fig. 1) the magnetizations tend to be tightly coupled to one another and oscillate about the static field direction. As the external radio-frequency or microwave field ($\boldsymbol{H}_{RF}$) increases the amplitude of the magnetization oscillations will increase. The torque introduced from the perpendicular radio or microwave frequency field $\boldsymbol{H}_{RF}$ will counteract the LLG damping torque that wants to align the magnetizations with the static field. In magnetic resonance experiments, one generally applies the oscillating (driving) field perpendicular to the static field because this counteracts the damping torque that wants to align the magnetization with the static field. In a typical ferromagnetic resonance (FR) experiment, resonance is observed when the energy taken from the driving field compensates for the damping energy of the magnetic specimen. In the antiferromagnetic case, when there is canting of the magnetizations, resonance can occur with the microwave field either parallel or perpendicular to the static field. We will examine both cases, but in Fig. 1 we have illustrated the case where the driving field is perpendicular to the applied field.

For the case of antiferromagnetic coupling (right side of Fig. 1), the magnetizations find their equilibrium positions when they are oriented opposite to one another, assuming the externally applied static field is weak compared to the coupling strength (this is the case illustrated in Fig. 1). As the static field strength increases, the magnetizations will become more aligned with the static field $\boldsymbol{H}_{\text{static}}$. Just as the case for ferromagnetic coupling, the application of an external driving field, $\boldsymbol{H}_{RF}$, will increase the amplitude of the magnetization oscillations. These descriptions represent the general features of the systems considered, but the true behavior of the magnetization dynamics is governed by the LLG equation [36] and corresponding energy density which we now discuss.

The energy density we consider in this paper is given by the sum of the Zeeman, demagnetization, and exchange coupling energies. There are other terms one may incorporate into the magnetic systems energy, for instance, uniaxial anisotropy or even higher order crystalline anisotropy terms, but our choices provide the simplest nontrivial results for the bilayer system. Such a situation could occur, for permalloy/Cu multilayers [37] or indeed many other multilayer combinations, for example Fe/Cu [38], which are grown by sputtering and where the coercive field is less than 15 Oe.

The Zeeman field is the sum of an external static field and oscillatory microwave field. The demagnetization field of both films provides anisotropy in the $\hat{\boldsymbol{y}}$ direction, which is representative of an easy-plane configuration. Exchange coupling of two magnetic layers through a nonmagnetic spacer has been observed for a large number of spacer materials [6,7,12,15] where the exchange interaction is propagated by itinerant electrons. This results in an oscillatory exchange coupling constant, J_{ex}, as the thickness of the spacer material is varied, thus allowing the sign and strength of the coupling to be tuned.

The energy density of the system is given by

$$E(\boldsymbol{M}^A, \boldsymbol{M}^B, t) = -\mu_0(\boldsymbol{M}^A d^A + \boldsymbol{M}^B d^B)\cdot \boldsymbol{H} + \frac{\mu_0}{2}\left[d^A\left(M_y^A\right)^2 + d^B\left(M_y^B\right)^2\right] - J_{ex}\frac{\boldsymbol{M}^A}{M_s^A}\cdot\frac{\boldsymbol{M}^B}{M_s^B}, \quad (1)$$

where μ_0 is the permeability of free space, $d^{\mathrm{A,B}}$ are the film thicknesses, $\boldsymbol{H} = \boldsymbol{H}_{\mathrm{static}} + \boldsymbol{H}_{RF}(t)$, and $M_s^{\mathrm{A,B}}$ are the saturation magnetizations. The form of the exchange coupling term is such that ferromagnetic coupling occurs for $J_{ex} > 0$ and antiferromagnetic coupling for $J_{ex} < 0$. Dimensional analysis on Eq. (1) shows that the energy density is given in energy per unit area ($\mathrm{J/m^2} = 1000\ \mathrm{erg/cm^2}$). In the hope that future experiments can be performed based on the results presented in this paper, we have used parameters typical of experimental investigations [6,7]. The exchange constant, J_{ex}, has been shown to vary from roughly -1 to 1 $\mathrm{erg/cm^2}$. The thicknesses we've explored are on the order of 1 nm and the saturation magnetization is on the order of 1.0×10^6 A/m ($4\pi M_s \approx 12.57$ kG) for both films. (Our analytic and numerical routines are formulated in the SI unit system, but we often show the field strengths and other parameters in CGS units when appropriate.)

The energy density leads to two coupled LLG equations through the effective field $\boldsymbol{H}_{\mathrm{eff}}^{\mathrm{A,B}} = -\boldsymbol{\nabla}_{\boldsymbol{M}}^{\mathrm{A,B}} E$, namely

$$\frac{d\boldsymbol{M}^{\mathrm{A,B}}}{dt} = -\frac{|\gamma^{\mathrm{A,B}}|}{1+(\alpha^{\mathrm{A,B}})^2}\left(\boldsymbol{M}^{\mathrm{A,B}}\times\boldsymbol{H}_{\mathrm{eff}}^{\mathrm{A,B}}\right) - \frac{|\gamma^{\mathrm{A,B}}|\alpha^{\mathrm{A,B}}}{M_s^{\mathrm{A,B}}[1+(\alpha^{\mathrm{A,B}})^2]}\times\left[\boldsymbol{M}^{\mathrm{A,B}}\times\left(\boldsymbol{M}^{\mathrm{A,B}}\times\boldsymbol{H}_{\mathrm{eff}}^{\mathrm{A,B}}\right)\right], \quad (2)$$

where $\boldsymbol{\nabla}_{\boldsymbol{M}}^{\mathrm{A,B}} = [1/(\mu_0 d^{\mathrm{A,B}} M_s^{\mathrm{A,B}})]\boldsymbol{\nabla}_{\boldsymbol{M}}$, $|\gamma^{\mathrm{A,B}}|$ is the gyromagnetic ratio, and $\alpha^{\mathrm{A,B}}$ is the damping constant. Even though we have written the equations of motion for differing magnetic films (i.e., using labels A and B for the different magnetic properties), much of our analysis is focused on coupled identical films. We have done this for two reasons: (1) It is important for the reader to understand the more general configuration, such that one can possibly expand on the results presented here, and (2) the nonlinear phenomenon we have observed is best understood by starting from a system with fewer parameter variations. With this said, we typically set $|\gamma^A| = |\gamma^B| \approx 2.31\times10^5\ \frac{1}{(\mathrm{A/m})\ \mathrm{s}}$ ($\approx 1.84\times10^7\ \frac{1}{\mathrm{Oe\ s}}$) and $\alpha^A = \alpha^B = 0.01$. The primary parameter variations we focus on in the current work are the drive amplitude (H_d) of the oscillatory microwave field, the exchange coupling constant J_{ex}, and the frequency of the microwave field ω_d.

We have solved Eqs. (1) and (2) numerically using a variety of integration schemes: standard fourth-order Runge-Kutta, explicit Runge-Kutta [39] of order (4)5, LSODA [40], and the midpoint method with second-order Adams-Bashforth extrapolation [41]. When the appropriate step size is chosen each numerical routine showed equivalent results. The magnitude of the magnetizations deviated the least using the midpoint method as described in Refs. [32,41].

III. LINEARIZATION AND DISPERSION RELATIONS

For small driving fields, the response of the magnetic bilayer system is found by linearizing the equations of motion [Eq. (2)] about the fixed points and solving for the resonant frequencies. The coupling between the two films results in two eigenmodes, an acoustic mode where the magnetizations oscillate in phase with one another and an optic mode where the magnetizations oscillate 180° out of phase. The acoustic and optic modes are not unique to the magnetic system and are observed in many other coupled systems (e.g., harmonic oscillators, pendula, phonons, etc.). What will be unique is the nonlinear behavior as the LLG equation differs from other systems.

When the films are ferromagnetically coupled ($J_{ex} > 0$) with an in-plane static field (as illustrated in Fig. 1), the equations of motion can be easily linearized in the limit of no damping, as the equilibrium configuration is oriented along the z axis. Setting $dM_z^A/dt = dM_z^B/dt = 0$ and keeping only first order terms in Eq. (2) results in the following matrix of coefficients for the eigenvalue equation of the remaining components $(M_x^A, M_y^A, M_x^B, M_y^B)$

$$X^F = \begin{bmatrix} 0 & |\gamma^A|\left(\frac{J}{\mu_0 d^A M_s^A} + H + M_s^A\right) & 0 & -|\gamma^A|\frac{J}{\mu_0 d^A M_s^B} \\ -|\gamma^A|\left(\frac{J}{\mu_0 d^A M_s^A} + H\right) & 0 & |\gamma^A|\frac{J}{\mu_0 d^A M_s^B} & 0 \\ 0 & -|\gamma^B|\frac{J}{\mu_0 d^B M_s^A} & 0 & |\gamma^B|\left(\frac{J}{\mu_0 d^B M_s^B} + H + M_s^B\right) \\ |\gamma^B|\frac{J}{\mu_0 d^B M_s^A} & 0 & -|\gamma^B|\left(\frac{J}{\mu_0 d^B M_s^B} + H\right) & 0 \end{bmatrix} \quad (3)$$

Assuming oscillatory solutions of the form $e^{i\omega t}$ and evaluating $\det(X^F - i\omega) = 0$ gives the eigenmodes of the ferromagnetically coupled system. The characteristic equation is a fourth order polynomial in quadratic form

$$\omega^4 + b\omega^2 + c = 0, \quad (4)$$

where

$$b = -(\gamma^A)^2\left[H^2 + \frac{2HJ}{\mu_0 d^A M_s^A} + HM_s^A + \left(\frac{J}{\mu_0 d^A M_s^A}\right)^2 - \frac{J}{\mu_0 d^A}\right] - (\gamma^B)^2\left[H^2 + \frac{2HJ}{\mu_0 d^B M_s^B} + HM_s^B + \left(\frac{J}{\mu_0 d^B M_s^B}\right)^2 - \frac{J}{\mu_0 d^B}\right] - \frac{2\gamma^A\gamma^B J^2}{\mu_0^2 d^A d^B M_s^A M_s^B} \quad (5)$$

and

$$c = (\gamma^A\gamma^B)^2\Bigg\{H^4 + 2H^3J\left(\frac{1}{\mu_0 d^A M_s^A} + \frac{1}{\mu_0 d^B M_s^B}\right) + H^3\left(M_s^A + M_s^B\right) + H^2J^2\left[\left(\frac{1}{\mu_0 d^B M_s^B}\right)^2 + \left(\frac{1}{\mu_0 d^A M_s^A}\right)^2\right]$$
$$+ H^2J\left(\frac{1}{\mu_0 d^A} + \frac{1}{\mu_0 d^B}\right) + 2H^2J\left(\frac{M_s^A}{\mu_0 d^B M_s^B} + \frac{M_s^B}{\mu_0 d^A M_s^A}\right) + H^2 M_s^A M_s^B$$
$$+ HJ^2\left(\frac{M_s^A}{\mu_0^2 (d^B)^2 \left(M_s^B\right)^2} + \frac{M_s^B}{\mu_0^2 (d^A)^2 \left(M_s^A\right)^2}\right) + HJ^2\left(\frac{1}{\mu_0^2 d^A d^B M_s^A} + \frac{1}{\mu_0^2 d^A d^B M_s^B}\right) + HJ\left(\frac{M_s^A}{\mu_0 d^B} + \frac{M_s^B}{\mu_0 d^A}\right)\Bigg\} \quad (6)$$

Solving for the eigenmodes of the antiferromagnetically coupled system ($J_{ex} < 0$) is more difficult because the equilibrium orientation of the magnetizations is now canted away from the principal axes. Fortunately, Smit and Beljers [13,42] derived a general method for performing such calculations in 1955. (Their method also works for the ferromagnetically coupled systems, but above we introduced the typical approach to linearization about a principal axis using Cartesian coordinates.) Their method exploits the fact that the torque on the magnetization can be written in terms of the gradient of the free energy density E [Eq. (1)]. Ignoring damping we have

$$\frac{d\boldsymbol{M}^{\mathrm{A,B}}}{dt} = -|\gamma^{\mathrm{A,B}}|[\boldsymbol{M}^{\mathrm{A,B}} \times (-\boldsymbol{\nabla}^{\mathrm{A,B}} E)]. \quad (7)$$

Using the coordinate system defined in Fig. 2, where the equilibrium orientation of the magnetization is along the $\hat{\boldsymbol{r}}$ direction and small deviations about the equilibrium are in the local $\hat{\boldsymbol{\theta}}$ and $\hat{\boldsymbol{\phi}}$ directions, the system constraints are such that the fixed points and eigenfrequencies can be found for arbitrary magnetic energy configurations. Writing the deviation of the magnetizations in these coordinates gives

$$\delta\boldsymbol{M}^{\mathrm{A,B}} = M_s^{\mathrm{A,B}}\hat{\boldsymbol{r}}^{\mathrm{A,B}} + M_s^{\mathrm{A,B}}\delta\theta^{\mathrm{A,B}}\hat{\boldsymbol{\theta}}^{\mathrm{A,B}} + M_s^{\mathrm{A,B}}\sin\theta^{\mathrm{A,B}}\delta\phi^{\mathrm{A,B}}\hat{\boldsymbol{\phi}}^{\mathrm{A,B}}, \quad (8)$$

where $\delta\theta^{\mathrm{A,B}}$ and $\delta\phi^{\mathrm{A,B}}$ are the small deviations about the equilibrium directions. The fixed points in these coordinates are given by $(\theta_0^A, \phi_0^A, \theta_0^B, \phi_0^B)$ and are found by setting Eq. (7) equal to zero, thus solving

$$\hat{\boldsymbol{r}}^{\mathrm{A,B}} \times \boldsymbol{\nabla}^{\mathrm{A,B}} E = 0$$
$$-\frac{1}{\sin(\theta^{\mathrm{A,B}})}\frac{\partial E}{\partial \phi_0^{\mathrm{A,B}}}\hat{\boldsymbol{\theta}}^{\mathrm{A,B}} + \frac{\partial E}{\partial \theta_0^{\mathrm{A,B}}}\hat{\boldsymbol{\phi}}^{\mathrm{A,B}} = 0. \quad (9)$$

Making the transformation of E $\rightarrow$ E$(\theta^A, \phi^A, \theta^B, \phi^B)$ and considering small deviations of the energy density

$$\delta E = \frac{\partial E}{\partial \theta_0^A}\delta\theta^A + \frac{\partial E}{\partial \phi_0^A}\delta\phi^A + \frac{\partial E}{\partial \theta_0^B}\delta\theta^B + \frac{\partial E}{\partial \phi_0^B}\delta\phi^B \quad (10)$$

one can linearize Eq. (7) and derive the following matrix of coefficients for ferromagnetic (X^F) or antiferromagnetic (X^{AF}) coupling

$$X^{F,\mathrm{AF}} = \begin{bmatrix} -\gamma_0^A\varepsilon_{\phi_0^A\theta_0^A} & -\gamma_0^A\varepsilon_{\phi_0^A\phi_0^A} & -\gamma_0^A\varepsilon_{\phi_0^A\theta_0^B} & -\gamma_0^A\varepsilon_{\phi_0^A\phi_0^B} \\ \gamma_0^A\varepsilon_{\theta_0^A\theta_0^A} & \gamma_0^A\varepsilon_{\theta_0^A\phi_0^A} & \gamma_0^A\varepsilon_{\theta_0^A\theta_0^B} & \gamma_0^A\varepsilon_{\theta_0^A\phi_0^B} \\ -\gamma_0^B\varepsilon_{\phi_0^B\theta_0^A} & -\gamma_0^B\varepsilon_{\phi_0^B\phi_0^A} & -\gamma_0^B\varepsilon_{\phi_0^B\theta_0^B} & -\gamma_0^B\varepsilon_{\phi_0^B\phi_0^B} \\ \gamma_0^B\varepsilon_{\theta_0^B\theta_0^A} & \gamma_0^B\varepsilon_{\theta_0^B\phi_0^A} & \gamma_0^B\varepsilon_{\theta_0^B\theta_0^B} & \gamma_0^B\varepsilon_{\theta_0^B\phi_0^B} \end{bmatrix}, \quad (11)$$

where

$$\gamma_0^A = \frac{|\gamma^A|}{\mu_0 d^A M_s^A \sin\theta_0^A}$$
$$\gamma_0^B = \frac{|\gamma^B|}{\mu_0 d^B M_s^B \sin\theta_0^B} \quad (12)$$

and

$$\varepsilon_{\phi_0^A\theta_0^A} = \frac{\partial^2 E}{\partial\phi_0^A\partial\theta_0^A}, \quad \varepsilon_{\phi_0^A\phi_0^A} = \ldots$$
$$\varepsilon_{\phi_0^B\theta_0^A} = \frac{\partial^2 E}{\partial\phi_0^B\partial\theta_0^A}, \quad \varepsilon_{\phi_0^B\phi_0^A} = \ldots. \quad (13)$$

Again, the dispersion relation is found by evaluating $\det(X^{F,\mathrm{AF}} - i\omega) = 0$ and solving for the eigenmode frequencies ω. The characteristic equation for ω reduces to

$$\omega^4 + b\omega^2 + c = 0, \quad (14)$$

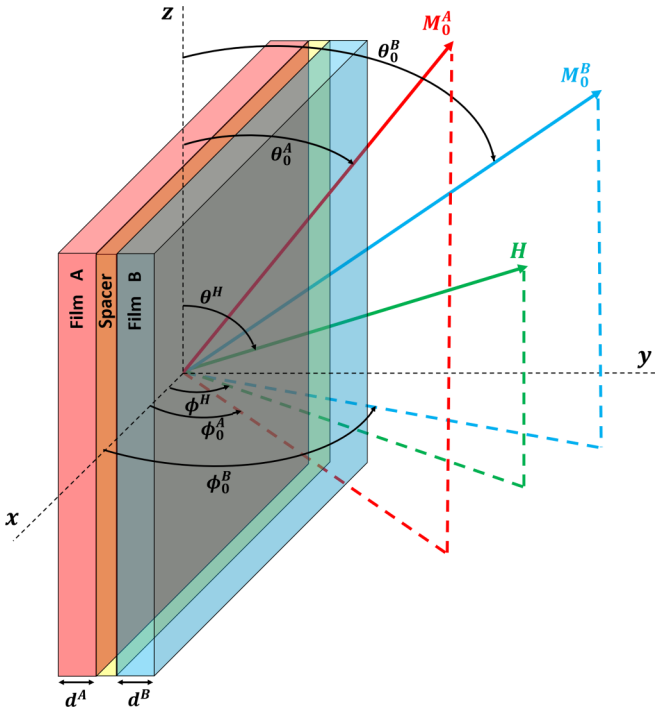

FIG. 2. Illustrative example of the equilibrium configuration in film A and B using the spherical coordinate system and an arbitrary orientation of the applied field $\boldsymbol{H}$. Linearization is carried out by considering small deviations about the fixed points $\boldsymbol{M}_0^A$ and $\boldsymbol{M}_0^B$.

where

$$b = \left(\gamma_0^A\right)^2\left(\varepsilon^2_{\phi_0^A\theta_0^A} - \varepsilon_{\phi_0^A\phi_0^A}\varepsilon_{\theta_0^A\theta_0^A}\right) + \left(\gamma_0^B\right)^2\left(\varepsilon^2_{\phi_0^B\theta_0^B} - \varepsilon_{\phi_0^B\phi_0^B}\varepsilon_{\theta_0^B\theta_0^B}\right) + 2\gamma_0^A\gamma_0^B\left(\varepsilon_{\phi_0^A\theta_0^B}\varepsilon_{\phi_0^B\theta_0^A} - \varepsilon_{\phi_0^A\phi_0^B}\varepsilon_{\theta_0^B\theta_0^A}\right) \tag{15}$$

and

$$\begin{aligned} c = \left(\gamma_0^A\gamma_0^B\right)^2\Big(&\varepsilon^2_{\phi_0^A\theta_0^A}\varepsilon^2_{\phi_0^B\theta_0^B} - \varepsilon^2_{\phi_0^A\theta_0^A}\varepsilon_{\phi_0^B\phi_0^B}\varepsilon_{\theta_0^B\theta_0^B} - \varepsilon_{\phi_0^A\theta_0^A}\varepsilon_{\phi_0^A\theta_0^B}\varepsilon_{\phi_0^B\theta_0^A}\varepsilon_{\phi_0^B\theta_0^B} + \varepsilon_{\phi_0^A\theta_0^A}\varepsilon_{\phi_0^A\theta_0^B}\varepsilon_{\phi_0^B\phi_0^B}\varepsilon_{\theta_0^B\theta_0^A} \\ &+ \varepsilon_{\phi_0^A\theta_0^A}\varepsilon_{\phi_0^A\phi_0^B}\varepsilon_{\phi_0^B\theta_0^A}\varepsilon_{\theta_0^B\theta_0^B} - \varepsilon_{\phi_0^A\theta_0^A}\varepsilon_{\phi_0^A\phi_0^B}\varepsilon_{\phi_0^B\theta_0^B}\varepsilon_{\theta_0^B\theta_0^A} - \varepsilon_{\phi_0^A\theta_0^A}\varepsilon_{\theta_0^A\theta_0^B}\varepsilon_{\phi_0^B\phi_0^A}\varepsilon_{\phi_0^B\theta_0^B} + \varepsilon_{\phi_0^A\theta_0^A}\varepsilon_{\theta_0^A\theta_0^B}\varepsilon_{\phi_0^B\phi_0^B}\varepsilon_{\theta_0^B\phi_0^A} \\ &+ \varepsilon_{\phi_0^A\theta_0^A}\varepsilon_{\theta_0^A\phi_0^B}\varepsilon_{\phi_0^B\phi_0^A}\varepsilon_{\theta_0^B\theta_0^B} - \varepsilon_{\phi_0^A\theta_0^A}\varepsilon_{\theta_0^A\phi_0^B}\varepsilon_{\phi_0^B\theta_0^B}\varepsilon_{\theta_0^B\phi_0^A} - \varepsilon_{\theta_0^A\theta_0^A}\varepsilon_{\theta_0^A\theta_0^A}\varepsilon^2_{\phi_0^B\theta_0^B} + \varepsilon_{\phi_0^A\phi_0^A}\varepsilon_{\theta_0^A\theta_0^A}\varepsilon_{\phi_0^B\phi_0^B}\varepsilon_{\theta_0^B\theta_0^B} \\ &+ \varepsilon_{\phi_0^A\phi_0^A}\varepsilon_{\theta_0^A\theta_0^B}\varepsilon_{\phi_0^B\theta_0^A}\varepsilon_{\phi_0^B\theta_0^B} - \varepsilon_{\phi_0^A\phi_0^A}\varepsilon_{\theta_0^A\theta_0^B}\varepsilon_{\phi_0^B\phi_0^B}\varepsilon_{\theta_0^B\theta_0^A} - \varepsilon_{\phi_0^A\phi_0^A}\varepsilon_{\theta_0^A\phi_0^B}\varepsilon_{\phi_0^B\theta_0^A}\varepsilon_{\theta_0^B\theta_0^B} + \varepsilon_{\phi_0^A\phi_0^A}\varepsilon_{\theta_0^A\phi_0^B}\varepsilon_{\phi_0^B\theta_0^B}\varepsilon_{\theta_0^B\theta_0^A} \\ &+ \varepsilon_{\phi_0^A\theta_0^B}\varepsilon_{\theta_0^A\theta_0^A}\varepsilon_{\phi_0^B\phi_0^A}\varepsilon_{\phi_0^B\theta_0^B} - \varepsilon_{\phi_0^A\theta_0^B}\varepsilon_{\theta_0^A\theta_0^A}\varepsilon_{\phi_0^B\phi_0^B}\varepsilon_{\theta_0^B\phi_0^A} + \varepsilon_{\phi_0^A\theta_0^B}\varepsilon_{\theta_0^A\phi_0^B}\varepsilon_{\phi_0^B\theta_0^A}\varepsilon_{\theta_0^B\phi_0^A} - \varepsilon_{\phi_0^A\theta_0^B}\varepsilon_{\theta_0^A\phi_0^B}\varepsilon_{\phi_0^B\phi_0^A}\varepsilon_{\theta_0^B\theta_0^A} \\ &- \varepsilon_{\phi_0^A\phi_0^B}\varepsilon_{\theta_0^A\theta_0^A}\varepsilon_{\phi_0^B\phi_0^A}\varepsilon_{\theta_0^B\theta_0^B} + \varepsilon_{\phi_0^A\phi_0^B}\varepsilon_{\theta_0^A\theta_0^A}\varepsilon_{\phi_0^B\theta_0^B}\varepsilon_{\theta_0^B\phi_0^A} - \varepsilon_{\phi_0^A\phi_0^B}\varepsilon_{\phi_0^B\phi_0^A}\varepsilon_{\phi_0^B\theta_0^A}\varepsilon_{\theta_0^B\phi_0^A} + \varepsilon_{\phi_0^A\phi_0^B}\varepsilon_{\theta_0^A\theta_0^B}\varepsilon_{\phi_0^B\phi_0^A}\varepsilon_{\theta_0^B\theta_0^A}\Big) \end{aligned} \tag{16}$$

In this coordinate system, a singularity occurs when the magnetization is along the z axis ($\theta^{A,B} = 0$), and that is another reason why earlier we introduced an alternative method for linearization using Cartesian coordinates. As the antiferromagnetic systems becomes saturated by the external static field along the $\hat{z}$ direction one may use Eqs. (4), (5), and (6) instead of Eqs. (14), (15), and (16) when evaluating the eigenmodes of the system.

Assuming the static field is along the $\hat{z}$ direction in the antiferromagnetic system, and using the energy density given by Eq. (1), one can derive an analytic expression for the canting angles (i.e., fixed points) of $\boldsymbol{M}^A$ and $\boldsymbol{M}^B$. The canting angles with respect to the z axis are given by:

$$\cos\left(\theta_0^A\right) = \frac{\left(J_{ex}M_s^Bd^B\right)^2 - \left(J_{ex}M_s^Ad^A\right)^2 - \left(\mu_0HM_s^Bd^BM_s^Ad^A\right)^2}{2J_{ex}\mu_0HM_s^Bd^B\left(M_s^Ad^A\right)^2} \tag{17}$$

$$\sin\left(\theta_0^B\right) = \frac{M_s^Ad^A}{M_s^Bd^B}\sin\left(\theta_0^A\right). \tag{18}$$

In the top panel of Fig. 3 we have plotted the canting angle as a function of the static field in the antiferromagnetic system for two different exchange constants. (We have assumed identical films and therefore the canting angle of both films with respect to the static field is the same $\theta_0^A = \theta_0^B$ = canting angle.) The dependency of the canting angle with respect to the static field reveals the balance between the exchange and Zeeman energies. Once the static field becomes strong enough, the magnetizations become saturated and the canting angle of the antiferromagnetic system goes to zero. As $J_{ex} \to 0^-$ the magnetizations become easier to align with the external static field, and as the exchange coupling becomes stronger the magnetizations find their equilibrium orientations further away from one another. Under strong exchange coupling a larger static field is needed to saturate the magnetizations along the static field direction.

In the middle and bottom panel of Fig. 3 we have plotted the resonant frequencies as a function of the static field for four different exchange coupling values. Two resonant frequencies are obtained for each field value due to the bilayer structure. In the ferromagnetic system (bottom panel) the optic mode is located at higher frequencies than the acoustic mode due to the additional torque added to the system when the magnetizations are not aligned [16]. A similar effect occurs in the antiferromagnetic system as well (middle panel), but when the static field becomes strong relative to the exchange coupling, the magnetization become more aligned with the static field and the optic mode frequency is located at a lower frequency than the acoustic mode. This crossover of the optic and acoustic modes occurs in the antiferromagnetic system when the canting angle is near 45°.

The optic mode varies less than the acoustic as the canting angle decreases from 90° to 45° because the magnetizations are oscillating nearly 180° out of phase, and therefore the in-plane or longitudinal components add while the transverse components tend to cancel. The optic mode appears at higher frequencies due to the additional torque added to the system when the magnetizations are not aligned [16].

The optic mode is of interest in the magnetism community [12] as one can possibly engineer an antiferromagnetic system at higher frequencies (compared to the acoustic mode) for use in electronic or signal processing [3] applications. In the following three sections we explore a number of interesting phenomena that arise from the nonlinear interactions in these coupled magnetic systems. In Sec. IV, we focus on the optic mode of a ferromagnetically coupled ($J_{ex} > 0$) system with a slight asymmetry in the drive amplitude, and in Sec. V, we show that the acoustic and optic mode can combine in the nonlinear limit to produce strong resonance responses at frequencies greater than the optic mode alone.

IV. NONLINEAR POWER-DEPENDENT LOCALIZATION FOR $J_{ex} > 0$

Approaching the nonlinear limit in the Schrödinger equation involves increasing the amplitude of the wave function. Similarly in the magnetic system, one can increase the precession angle. This can be accomplished by setting an initial direction for the spins, or by increasing the drive amplitude (H_d) of the external driving microwave field $\boldsymbol{H}_{RF}(t) = H_d\cos(\omega_d t)\hat{\boldsymbol{x}}$. In this paper we take the driving field to be linearly polarized along the $\hat{\boldsymbol{x}}$ direction (excluding the case described later for Fig. 16), as experimentally, one could construct such a configuration in a microstrip waveguide to drive the films with large amplitude magnetic fields. As one reduces

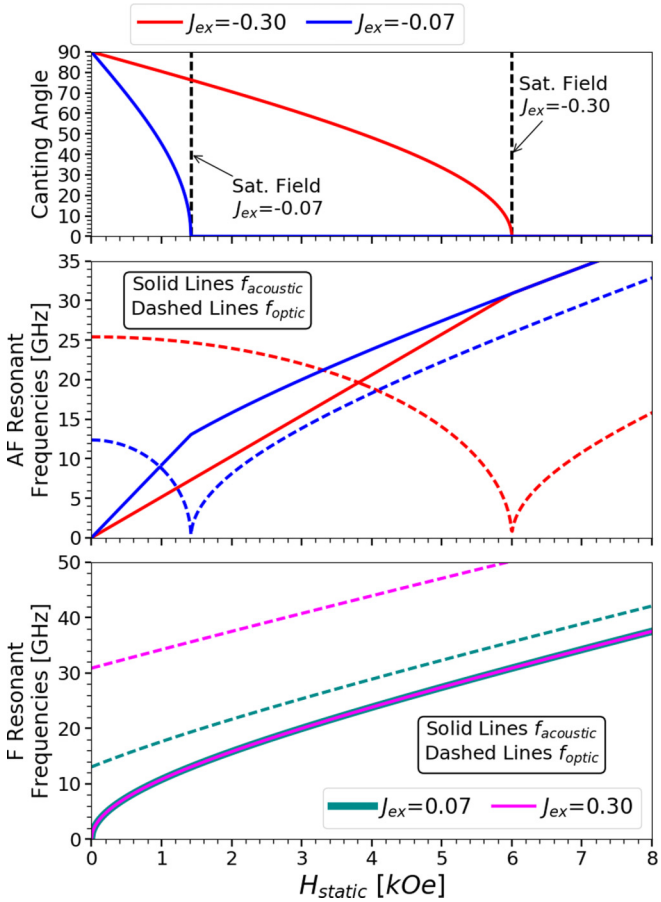

FIG. 3. Top panel: Canting angle as a function of the static field for two different AF exchange coupling constants. Middle panel: Acoustic and optic mode resonant frequencies as a function of the static field for two different AF exchange coupling constants. Bottom panel: Acoustic and optic mode resonant frequencies as a function of the static field for two different F exchange coupling constants. The exchange constants (J_{ex}) are in units of erg/cm^2. The saturation (Sat.) field values for the two AF exchange values ($J_{ex} < 0$) are shown by the vertical dashed-black lines in the top panel. The remaining parameters used are $d^A = d^B = 1$ nm, $|\gamma^A| = |\gamma^B| \approx 2.31 \times 10^5 \frac{1}{(\text{A/m})\ \text{s}}$ ($\approx 1.84 \times 10^7 \frac{1}{\text{Oe s}}$), and $M_s^A = M_s^B = 1.0 \times 10^6$ A/m ($4\pi M_s \approx 12.57$ kG).

the size of a microstrip waveguide, while keeping the input power constant, one can achieve large amplitude microwave fields (over 200 Oe) in a magnetic film sample [24,25]. Using the Poynting vector, one can show that the strength of the magnetic field in the microstrip configuration is proportional to the $\sqrt{power/area}$, thus, reducing the dimensions of the waveguide leads to larger microwave fields. This has been reported in Ref. [24] where the authors used a high frequency structure simulator to calculate the strength of the oscillating magnetic field along the $\hat{\boldsymbol{x}}$ direction. Large gradients in the simulations reveal that a magnetic bilayer sample may have different drive amplitudes in each film, and we explore some consequences of this in what follows.

When $J_{ex} > 0$ (ferromagnetic coupling) the equilibrium directions of the magnetization in each film are parallel to the applied static field. The addition of slightly differing drive amplitudes across the two identical films breaks the symmetry

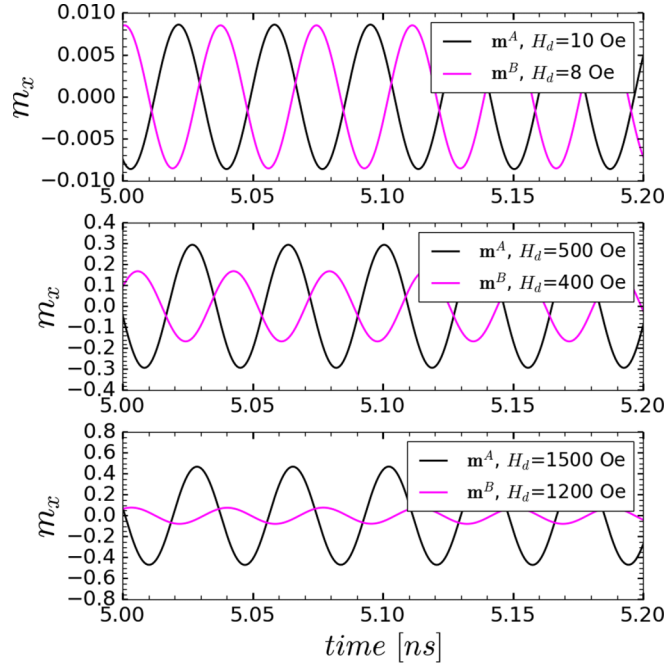

FIG. 4. m_x components of the magnetizations for different drive amplitudes. Top panel: In the linear limit the magnetizations are nearly 180° out of phase. Middle panel: In the nonlinear limit the magnetizations become phase shifted and m_x^B amplitude is reduced. Bottom panel: Further increasing the drive amplitude leads to a strong localization in film A. The parameters of the simulations are $f_d \approx 27.14$ GHz, $J_{ex} \approx 0.78$ erg/cm^2, $|\gamma^A| = |\gamma^B| \approx 2.31 \times 10^5 \frac{1}{(\text{A/m})\ \text{s}}$ ($\approx 1.84 \times 10^7 \frac{1}{\text{Oe s}}$), $M_s^A = M_s^B = 1.0 \times 10^6$ A/m ($4\pi M_s \approx 12.57$ kG), $d^A = d^B = 4$ nm, $\alpha^A = \alpha^B = 0.01$, $H_{\text{static}} \approx 7.96 \times 10^4$ A/m (1000 Oe).

and different behaviors can be observed. In the examples we present here, we have let $H_d^B = 0.8 H_d^A$ (for the ferromagnetic coupling only) and show that localized magnetization oscillations can occur at either acoustic or optic mode frequencies. The asymmetry in the drive amplitudes across the films leads to a power-dependent localization of the magnetization oscillations in one film or the other depending on the exchange coupling, drive amplitude, and driving frequency.

In the first example shown in Fig. 4, we have plotted the m_x (m_x is the normalized magnetization in the $\hat{\boldsymbol{x}}$ direction $m_x = M_x/M_s$) component of both films for different drive amplitudes when driven at the optic mode frequency ($f_d \approx 27.14$ GHz). (The m_y and m_z components are not provided for simplicity, and because the system is being driven along the $\hat{\boldsymbol{x}}$ direction, the m_x component provides an adequate interpretation of the magnetization precession in response to the driving field.) The top panel of Fig. 4 shows both magnetizations of equal magnitude oscillating nearly 180° out of phase in the linear low field limit ($H_d = 10$ Oe). The lower two panels of Fig. 4 show that as the microwave field increases in magnitude, the oscillations become primarily localized in film A, while the amplitude of oscillations in film B are reduced. In addition, there is a slight change in the phase difference between the magnetizations.

The power-dependent localization is further illustrated over a broad range of drive amplitudes for different exchange

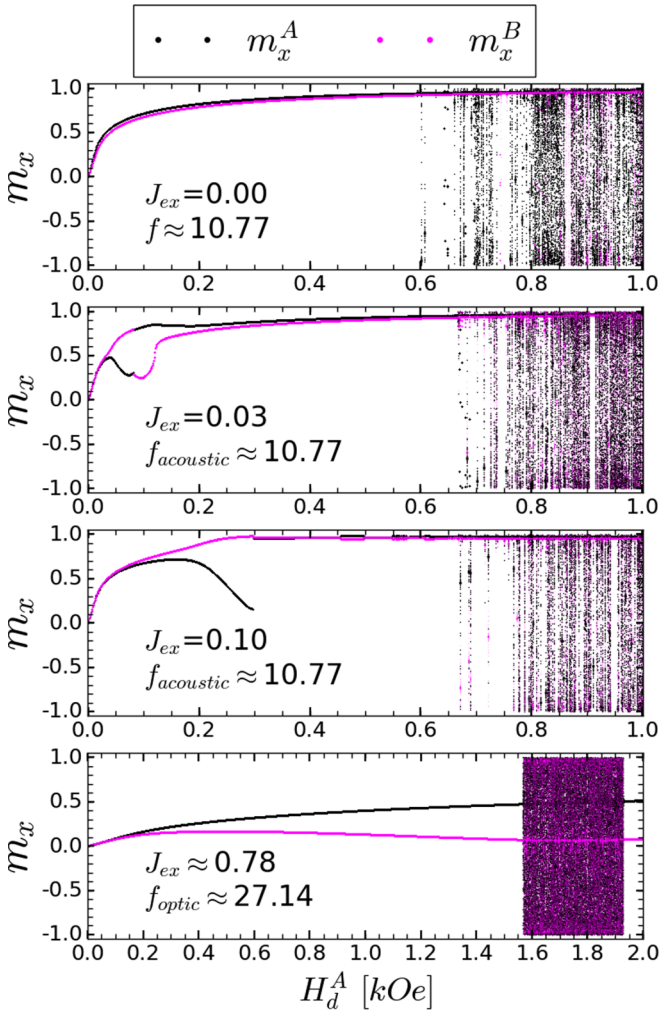

FIG. 5. One hundred Poincaré sections at each value of H_d^A at the maximum of the component oscillations 10 ns after the simulation has initialized (i.e., bifurcation diagram). The asymmetry introduced in the drive amplitudes ($H_d^B = 0.8H_d^A$) allows the component oscillations to become localized as the driving field is increased. J_{ex} and f are in units of erg/cm^2 and GHz, respectively. The parameters of the simulations are $|\gamma^A| = |\gamma^B| \approx 2.31 \times 10^5 \frac{1}{(\mathrm{A/m})\ \mathrm{s}}$ ($\approx 1.84 \times 10^7 \frac{1}{\mathrm{Oe\ s}}$), $M_s^A = M_s^B = 1.0 \times 10^6$ A/m ($4\pi M_s \approx 12.57$ kG), $d^A = d^B = 4$ nm, $\alpha^A = \alpha^B = 0.01$, $H_{\mathrm{static}} \approx 7.96 \times 10^4$ A/m (1000 Oe).

coupling and two different drive frequencies in the bifurcation diagram of Fig. 5. In this form of a bifurcation diagram we have taken 100 Poincaré sections at each value of the drive amplitude (H_d^A) at the maximum of the component oscillations 10 ns after the simulation has initialized. This ensures we are not picking up the initial transient behavior and $m_x^{\mathrm{A,B}}$ represents the peak amplitude of magnetization oscillations for the films. When there appears to be only one point for a given value of the drive amplitude and film label (A or B), the magnetization is under period-one motion. If there is a continuum of points for a particular drive amplitude the motion may, in principle, be quasiperiodic or chaotic.

The top panel (first panel) of Fig. 5 shows the peak amplitude of oscillation as a function of the drive amplitude in the limit of no exchange coupling at the resonant frequency (acoustic mode) of the system ($f = 10.77$ GHz). Here, each film undergoes period-one motion, and $m_x^{\mathrm{A,B}}$ increases with increasing H_d^A from $0 \rightarrow 0.6$ kOe. There is little difference between m_x^A and m_x^B until the systems starts showing signs of chaotic behavior near 0.6 kOe. In the second panel, where we have turned on the ferromagnetic exchange coupling ($J_{ex} = 0.03$ erg/cm^2), the peak components of m_x^A and m_x^B begin to diverge from one another near $H_d = 30$ Oe. From $H_d = 30 \rightarrow 81$ Oe the oscillations are primarily localized in film B. Somewhere between 81 and 82 Oe the system reverses its behavior and the localization occurs in film A. Further increasing H_d causes the localization to disappear. (The second panel shows period-one motion of each film from approximately $0 \rightarrow 650$ Oe). The third panel shows that by increasing the exchange coupling to $J_{ex} = 0.10$ erg/cm^2 the system can lead to a more dramatic localization behavior, but the reversal or switching behavior between the films is not present. Finally, the fourth (bottom) panel shows that when the system is driven at the optic mode frequency the localization occurs only in film A, and the system's response to the driving field is reduced compared to that of the acoustic frequency. (The fourth panel uses the same parameters as that shown for Fig. 4). As H_d^A is increased above 1 kOe in the top three panels the behavior is primarily chaotic. In the bottom panel with stronger coupling and higher driving frequency, the motion is chaotic from roughly $H_d = 1.57 \rightarrow 1.93$ kOe, then transitions back to period one motion above 1.93 kOe. Similar behaviors are observed for different drive amplitude asymmetries (e.g., $H_d^B = 0.9H_d^A$ and $H_d^B = 0.7H_d^A$) as well as different exchange coupling (e.g., $J_{ex} = 0.05$, 0.07, and 0.40 erg/cm^2). We have not characterized the localization behavior over the entirety of the parameter space, but we have shown that its occurrence is connected with the drive amplitude asymmetry and occurs for a number of parameter variations.

We note that values of oscillating fields in the 100–200 Oe range have been experimentally realized in microstrip structures where the characteristic lengths (signal line width and dielectric thickness) are on the order of microns. However, based on the calculations indicated in Ref. [25], smaller microstrip structures, with dimensions on the order of a few hundred nanometers, could produce substantially larger microwave fields, in the 1000–3000 Oe range.

It turns out this power-dependent localization is easy to understand. Localization, for example, is also observed in the linear limit when the films are driven slightly (a few GHz) off the optic mode frequency. In the linear limit ($H_d \approx 10$ Oe), increasing or decreasing the driving frequency from that of the optic mode leads to localization in one film or the other and a phase shift. For example, with $H_d \approx 10$ Oe and using the parameters in the caption of Fig. 4 ($f_d = f_{\mathrm{optic}} \approx 27.14$ GHz) no localization is observed (see top panel of Fig. 4), but increasing the drive frequency to $f_d \approx 29.14$ GHz leads to a localization in film A, while decreasing the drive frequency to $f_d \approx 25.14$ GHz leads to localization in film B. It is well known that in most nonlinear dynamic systems the resonant frequencies shift when strongly driven. In this case, the localization observed in Fig. 4 and the bottom panel (fourth panel) of Fig. 5 is a result of the nonlinear optic mode frequency shifting to a lower value when strongly driven, and therefore, leading to a localization in film A (i.e., having

$f_d > f_{\text{optic}}$ in the nonlinear regime leads to a localization in film A).

Localization is also observed near the acoustic mode frequency as we highlighted in Fig. 5 but only for weaker exchange coupling. In addition, the localization behavior in the linear limit is opposite from that of the optic mode when driven at frequencies near the acoustic mode (i.e., $f_d > f_{\text{acoustic}}$ leads to localization in film B, while $f_d < f_{\text{acoustic}}$ leads to localization in film A). Therefore in the case of the acoustic mode, having $f_d > f_{\text{acoustic}}$ in the nonlinear regime leads to localization in film B. This is clearly observed in the third panel of Fig. 5.

We comment on the unique behavior seen in the second panel of Fig. 5 ($J_{ex} = 0.03$ erg/cm^2), where the localization reverses as the driving amplitude is increased. For the small exchange coupling considered here the optic mode is within 1 GHz of the acoustic mode ($f_{\text{acoustic}} \approx 10.77$ GHz, $f_{\text{optic}} \approx 11.62$ GHz). As the drive amplitude is increased, there is a critical value at which the films switch their behaviors. The critical drive amplitude occurs when the nonlinear optic mode frequency shifts below f_d.

We present a second example of localization that is more closely related to the quantum system we referred to in the introduction. We consider a magnetic coupled system with no damping or driving field, thereby strictly focusing on the interplay between the exchange coupling and static field strength. In Fig. 6 we examine this case in the linear (top panel) and nonlinear (bottom panel) limits. The linear limit of this system is given by considering a small deviation of the magnetizations about the static field direction ($\boldsymbol{H}_{\text{static}} = 1000\ \text{Oe}\,\hat{\boldsymbol{z}}$), where we have let $\theta_0^A = 0.1$ and $\theta_0^B = 0.0$. This linear limit configuration results in the back and forth switching of oscillatory behavior from one film to the other (i.e., the energy is sloshing from one film to the other). Note that if the magnetizations were precisely aligned with the static field ($\theta_0^A = \theta_0^B = 0.0$), no oscillation would occur at all, as there is no torque introduced to set the system in motion. In the nonlinear limit, where we have let $\theta_0^A = 1.2$ and $\theta_0^B = 0.0$, the energy is not fully transferred from one film to the other, and therefore localized magnetization oscillations can occur. The threshold for when localization occurs in this system is a function of the initial conditions ($\theta_0^A, \phi_0^A, \theta_0^B, \phi_0^B$), exchange coupling, and the strength of the static field. For example, using the parameters provided in the caption of Fig. 6, localization is not observed until $\theta_0^A \gtrsim 0.9$ radians.

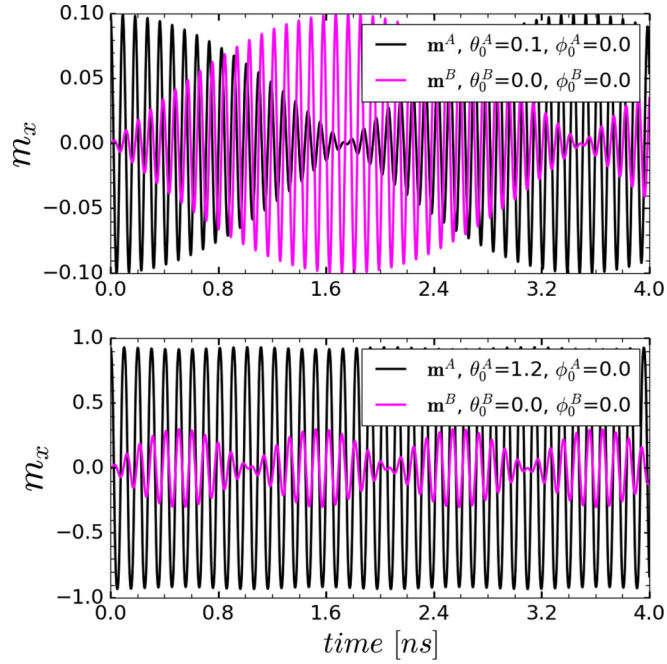

FIG. 6. m_x components of the magnetizations with no damping and driving field for different initial conditions. The units of the initial conditions are radians. Top panel: Exchange coupling between the films in the linear limit leads to the back and forth transfer of energy from one film to the other. Bottom panel: In the nonlinear limit the exchange coupling is not strong enough for the complete transfer of energy from one film to the other, and therefore, the oscillations become localized in film A. The simulation parameters are $J_{ex} \approx 0.01$ erg/cm^2, $d^A = d^B = 4$ nm, $|\gamma^A| = |\gamma^B| \approx 2.31 \times 10^5 \frac{1}{(\text{A/m})\ \text{s}}$ ($\approx 1.84 \times 10^7 \frac{1}{\text{Oe s}}$), $M_s^A = M_s^B = 1.0 \times 10^6$ A/m ($4\pi M_s \approx 12.57$ kG), $\alpha^A = \alpha^B = 0$, and $H_{\text{static}} \approx 7.96 \times 10^4$ A/m (1000 Oe).

V. NONLINEAR COUPLING OF THE ACOUSTIC AND OPTIC MODE IN THE ANTIFERROMAGNETIC SYSTEM

Nanoscale magnetic devices with high operational frequencies are of interest to many researchers [12,15,34,43]. Here we discuss an interesting high-frequency nonlinear mode that arises in the antiferromagnetic exchange-coupled bilayer system. Over the parameter space we've investigated the mode appears to be tunable from 20 to 50 GHz, depending on the exchange coupling and static field strength.

Using the antiferromagnetic bilayer configuration shown in Fig. 1 and the energy density given by Eq. (1), but simply changing the sign of the exchange coupling constant ($J_{ex} < 0$), leads to dramatically different behavior compared to that discussed in Sec. IV. The energy landscape now favors the magnetization in the layers to be canted away from each other, with the canting angles governed by the strength of the exchange coupling and the static field for identical films. [The more general configuration angles are given by Eqs. (17) and (18) in Sec. III.]

In this section we focus on antiferromagnetic resonance (AFR) calculations to guide our inquires into the AF bilayer system. The numerical AFR calculations start by specifying the material parameters ($|\gamma^A|$, $|\gamma^B|$, M_s^A, M_s^B, J_{ex}, α^A, α^B, d^A, d^B, film area), a fixed static field along the $\hat{\boldsymbol{z}}$ direction, then applying a transverse oscillatory microwave field $\boldsymbol{H}_{RF}(t) = H_d \cos(2\pi f_d t)\ \hat{\boldsymbol{x}}$ and sweeping over a range of frequencies (f_d). For each frequency, we run our LLG dynamics calculations from time zero to 100 or more drive periods past a 10 ns simulation time. (This ensures we are not picking up the initial transient behavior.) We then calculate the power absorbed per unit volume from the microwave field at each time step, indexed by i, from 10 ns to 100 drive periods later for each layer $P_i^A = 0.5\mu_0(H_{d_i} \cdot d\boldsymbol{M}_i^A/dt)$ (similarly for P_i^B). Sum the two quantities $P_{\text{tot}_i} = P_i^A + P_i^B$ for each time step and then calculate the time-averaged power $\langle P \rangle = \Sigma P_{\text{tot}_i} dt_i/\Delta t$ over the 100 drive period time interval (Δt). This result is then normalized to the time-averaged input power $0.5\mu_0(H_d)^2\omega_d$ over the same

time interval. This numerical procedure leads to the normalized (Norm.) power absorbed as a function of the frequency as shown in Fig. 7. Figure 7 reveals the strength of the FR and AFR response to an oscillatory driving field, where the peaks indicate the resonant frequencies of the magnetic system.

In the linear limit, the normalized power absorbed can be derived analytically from the LLG equation [Eq. (2)], and one finds that coefficients of the dynamic magnetization are directly proportional to the drive field amplitude through the dynamic or AC susceptibility $\chi = \chi' + i\chi''$ [14,44,45]. The imaginary part of the susceptibility is related to microwave absorption, and this allows us to test our numerical scheme for calculating the normalized power absorbed with an analytic formula for the susceptibility. Using the LLG equation for a single magnetic film with $\boldsymbol{H}_{\text{eff}} = H_d(t)\hat{x} - M_y\hat{y} + H\hat{z}$, one can show that

$$\chi'' = \frac{M\alpha\omega|\gamma|(1+\alpha^2)[|\gamma|^2(1+\alpha^2)(H+M)^2 + \omega^2(1+\alpha^2)^2]}{H^2|\gamma|^4(H+M)^2(1+\alpha^2)^2 - |\gamma|^2\omega^2(1+\alpha^2)^2[2H(H+M) - \alpha^2(2H^2+2HM+M^2)] + \omega^4(1+\alpha^2)^4} \tag{19}$$

where H is the static field and M is the saturation magnetization. Using Eq. (19) with $|\gamma| \approx 2.31 \times 10^5 \frac{1}{(\text{A/m})\,\text{s}}$, $M = 1.0 \times 10^6$ A/m, $H \approx 7.96 \times 10^4$ A/m, and $\alpha = 0.01$ results in a peak susceptibility of 317.79 at a frequency of 10.77 GHz. Numerically, using the procedure outlined above for the normalized absorbed power, and with a 1 Oe (≈79.58 A/m) drive amplitude, we arrive at $\chi'' \approx 317.79$. These results provide some confidence in our numerical routines for calculating χ'' or normalized power absorbed in the nonlinear regimes.

As mentioned earlier, we are primarily focused on identical films where there are no thickness imbalances ($d^A = d^B$), saturation differences ($M_s^A = M_s^B$), gyromagnetic ratio differences ($|\gamma^A| = |\gamma^B|$), or damping differences ($\alpha^A = \alpha^B$). We will briefly discuss excursions from the identical film limit when appropriate, as in the real world perfectly identical films are not likely.

In Fig. 7 we present the AFR response when $J_{ex} = -0.30$ erg/cm^2 and $H_{\text{static}} = 1000$ Oe for two different drive amplitudes, $H_d = 10$ Oe (linear regime) and $H_d = 200$ Oe (nonlinear regime). We have also included the FR response (labeled with F in the figure) when $J_{ex} = 0.30$ erg/cm^2 as an added comparison between the systems. The four black arrows along the frequency axis are the linear eigenfrequencies derived from solving for ω in Eqs. (4), (5), and (6) and Eqs. (14), (15), and (16). In the linear limit only the two acoustic modes ($f^{\text{AF}}_{\text{acoustic}}$ and f^{F}_{acoustic}) absorb energy. The optic mode resonances are not observable in this limit due to

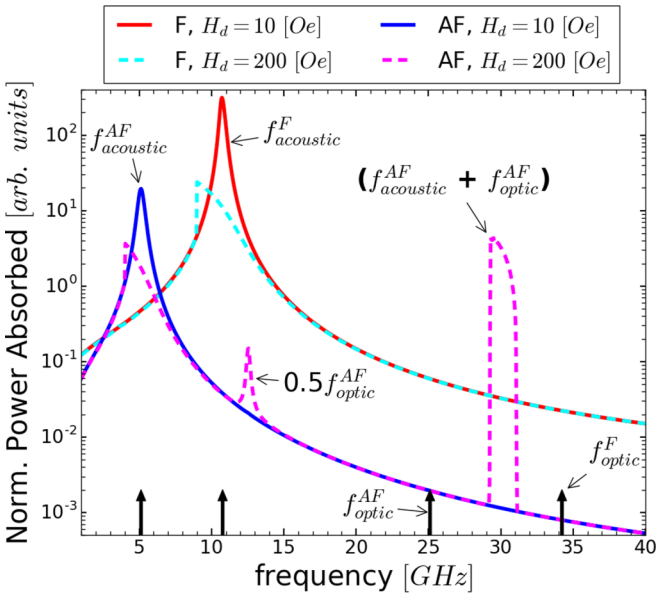

FIG. 7. Numerical AFR and FR responses for identical films in the linear and nonlinear regimes. The ferromagnetic (F) bilayer resonances are shown by the solid-red and dashed-cyan curves for $J_{ex} = 0.30$ erg/cm^2, while the antiferromagnetic (AF) bilayer resonances are shown by the solid-blue and dashed-magenta curves for $J_{ex} = -0.30$ erg/cm^2. The remaining simulation parameters are $|\gamma^A| = |\gamma^B| \approx 2.31 \times 10^5 \frac{1}{(\text{A/m})\,\text{s}}$ ($\approx 1.84 \times 10^7 \frac{1}{\text{Oe s}}$), $M_s^A = M_s^B = 1.0 \times 10^6$ A/m ($4\pi M_s \approx 12.57$ kG), $d^A = d^B = 1$ nm, $\alpha^A = \alpha^B = 0.01$, $H_{\text{static}} \approx 7.96 \times 10^4$ A/m (1000 Oe).

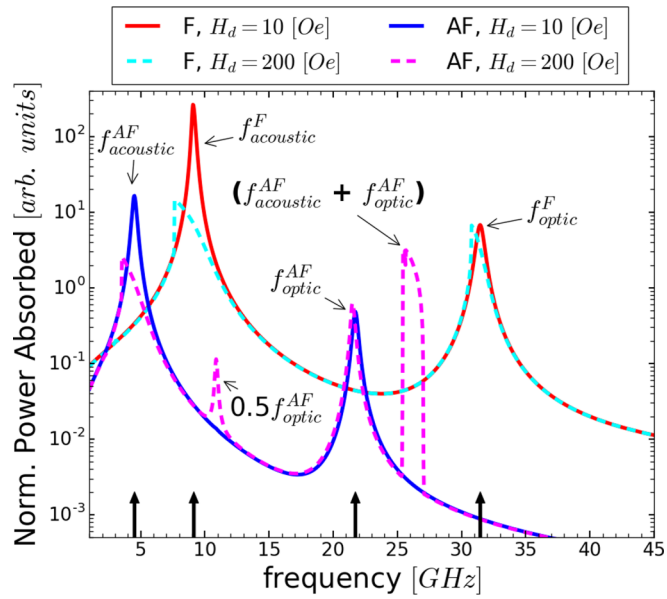

FIG. 8. Numerical AFR and FR responses for different saturation magnetizations and unequal film thicknesses in the linear and nonlinear regimes. The ferromagnetic (F) bilayer resonances are shown by the solid-red and dashed-cyan curves for $J_{ex} = 0.30$ erg/cm^2, while the antiferromagnetic (AF) bilayer resonances are shown by the solid-blue and dashed-magenta curves for $J_{ex} = -0.30$ erg/cm^2. The simulation parameters are $|\gamma^A| = |\gamma^B| \approx 2.31 \times 10^5 \frac{1}{(\text{A/m})\,\text{s}}$ ($\approx 1.84 \times 10^7 \frac{1}{\text{Oe s}}$), $M_s^A = 1.0 \times 10^6$ A/m ($4\pi M_s^A \approx 12.57$ kG), $M_s^B = 5.0 \times 10^5$ A/m ($4\pi M_s^B \approx 6.28$ kG), $d^A = 1$ nm, $d^B = 2$ nm, $\alpha^A = \alpha^B = 0.01$, $H_{\text{static}} \approx 7.96 \times 10^4$ A/m (1000 Oe).

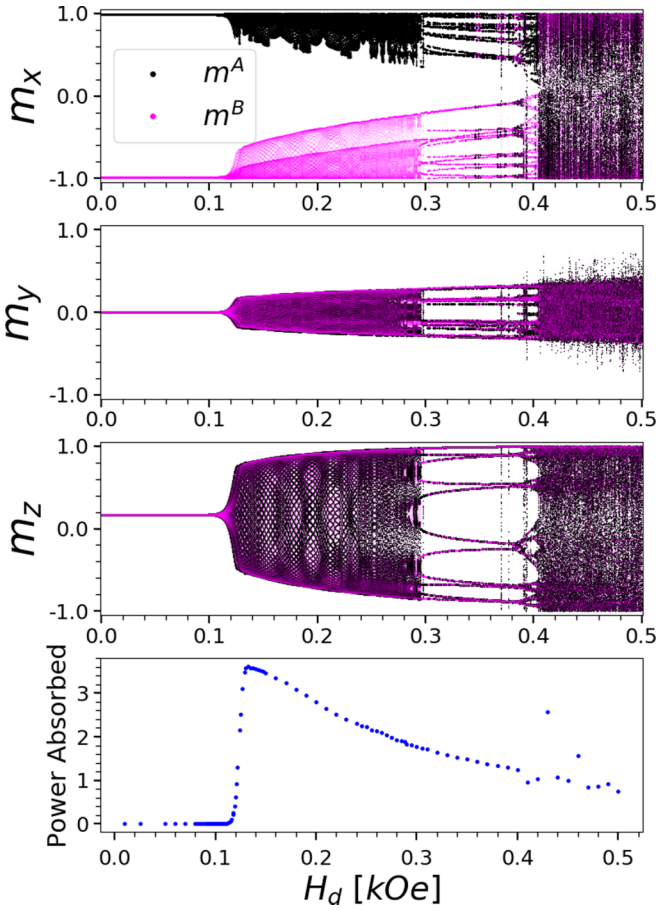

FIG. 9. Bifurcation diagram (top 3 panels) and the normalized power absorbed (AFR response) at the acoustic plus optic mode frequency ($f_{\text{acoustic}} + f_{\text{optic}}$). The bifurcation diagram has four distinct regions. 0–105 Oe: period-one motion. 105–300 Oe: quasiperiodic motion. 300–370 Oe: multiperiodic motion. 370–500 Oe: primarily chaotic motion. Bottom panel: the transition from period-one to quasiperiodic behavior leads to a large increase in the AFR response. The simulation parameters are $J_{ex} = -0.30$ erg/cm^2, $f_d \approx 30.2$ GHz, $|\gamma^A| = |\gamma^B| \approx 2.31 \times 10^5 \frac{1}{(\text{A/m})\ \text{s}}$ ($\approx 1.84 \times 10^7 \frac{1}{\text{Oe s}}$), $M_s^A = M_s^B = 1.0 \times 10^6$ A/m ($4\pi M_s \approx 12.57$ kG), $d^A = d^B = 1$ nm, $\alpha^A = \alpha^B = 0.01$, $H_{\text{static}} \approx 7.96 \times 10^4$ A/m (1000 Oe).

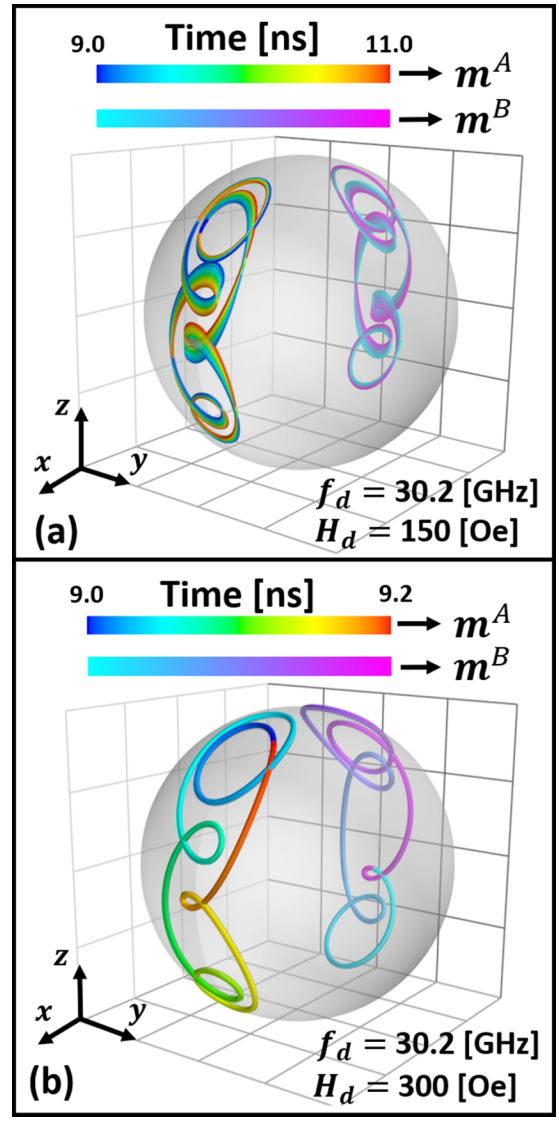

FIG. 10. Quasiperiodic and period-six attractors that illustrate the antiferromagnetic magnetization dynamics within certain regions of the bifurcation diagram of Fig. 9. (a) Quasiperiodic attractors from 9.0 to 11.0 ns (60 drive periods) when $H_d = 150$ Oe. Period-six attractors from 9.0 to 9.2 ns (6 drive periods) when $H_d = 300$ Oe. The simulation parameters are $J_{ex} = -0.30$ erg/cm^2, $f_d \approx 30.2$ GHz, $|\gamma^A| = |\gamma^B| \approx 2.31 \times 10^5 \frac{1}{(\text{A/m})\ \text{s}}$ ($\approx 1.84 \times 10^7 \frac{1}{\text{Oe s}}$), $M_s^A = M_s^B = 1.0 \times 10^6$ A/m ($4\pi M_s \approx 12.57$ kG), $d^A = d^B = 1$ nm, $\alpha^A = \alpha^B = 0.01$, $H_{\text{static}} \approx 7.96 \times 10^4$ A/m (1000 Oe).

the films having identical magnetic properties. As the drive amplitude further increases from 10 Oe, the acoustic mode resonances decrease in amplitude and start to shift toward lower frequencies due to the increased precession angle. In the nonlinear limit ($H_d = 200$ Oe), there are no new absorption peaks that appear in the F system, while in the AF system two new peaks arise: one relatively weak mode at $0.5 f_{\text{optic}}^{\text{AF}}$ and a strong high-frequency mode centered around the acoustic plus optic mode frequency ($f_{\text{acoustic}}^{\text{AF}} + f_{\text{optic}}^{\text{AF}}$).

There are a number of unique features in connection with the spontaneous appearance of this high-frequency absorption peak. First, it is surprising that a high-frequency composite mode (acoustic plus optic) can have a response as large as or larger than the low frequency acoustic mode. Second, it is surprising that the new absorption peak has a frequency involving the $f_{\text{optic}}^{\text{AF}}$ when there is no absorption at the frequency of the optic mode. It may be possible to observe this behavior in an experiment and possibly exploit the behavior in a device, such as a power limiter.

The composite mode that arises in this magnetic bilayer system is not restricted to the system of identical films and continues to appear for many different parameter variations of the AF system. The composite mode does appear to be unique to the AF system, as we have yet to observe it in the F system over the parameter space we have investigated. Figure 8 illustrates the resonant modes when the films have differing magnetic properties (namely the saturation magnetization) and film thicknesses. One should notice that Fig. 8 has many

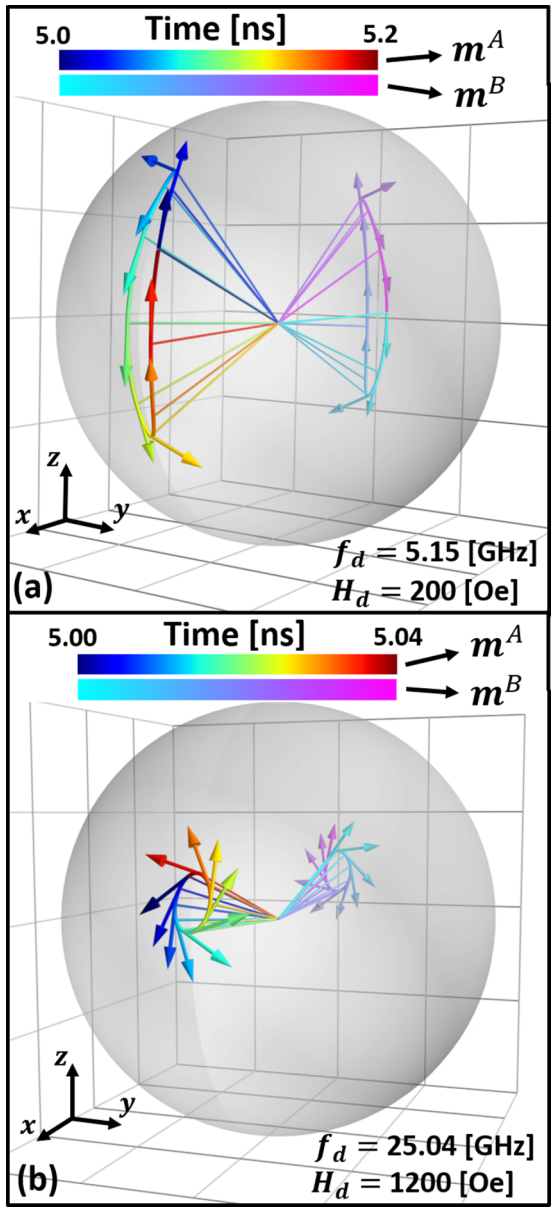

FIG. 11. Late-time magnetization trajectories (attractors) at the fundamental acoustic ($f^{\mathrm{AF}}_{\mathrm{acoustic}} = 5.15$ GHz) and optic ($f^{\mathrm{AF}}_{\mathrm{optic}} = 25.04$ GHz) mode for two different drive amplitudes. (a) Acoustic mode. (b) Optic mode (to visualize the optic mode on the unit sphere the drive amplitude was increased significantly over the acoustic mode). The color gradients indicate the time evolution, while the arrows indicate the direction of $d\boldsymbol{m}^{\boldsymbol{A,B}}/dt$ at a few points along the trajectory. The simulation parameters are $J_{ex} = -0.30$ erg/cm^2, $|\gamma^A| = |\gamma^B| \approx 2.31 \times 10^5 \frac{1}{(\mathrm{A/m})\ \mathrm{s}}$ ($\approx 1.84 \times 10^7 \frac{1}{\mathrm{Oe\ s}}$), $M^A_s = M^B_s = 1.0 \times 10^6$ A/m ($4\pi M_s \approx 12.57$ kG), $d^A = d^B = 1$ nm, $\alpha^A = \alpha^B = 0.01$, $H_{\mathrm{static}} \approx 7.96 \times 10^4$ A/m (1000 Oe).

of the same features as Fig. 7, but the optic modes of both the AF and F system now appear and the resonant frequencies have shifted to slightly lower values. The composite mode is still present in Fig. 8 when the saturation magnetizations differ and would be present even if there was only a thickness imbalance.

The AF system is highly sensitive to thickness imbalances as the fixed points of the system change according to Eqs. (17)

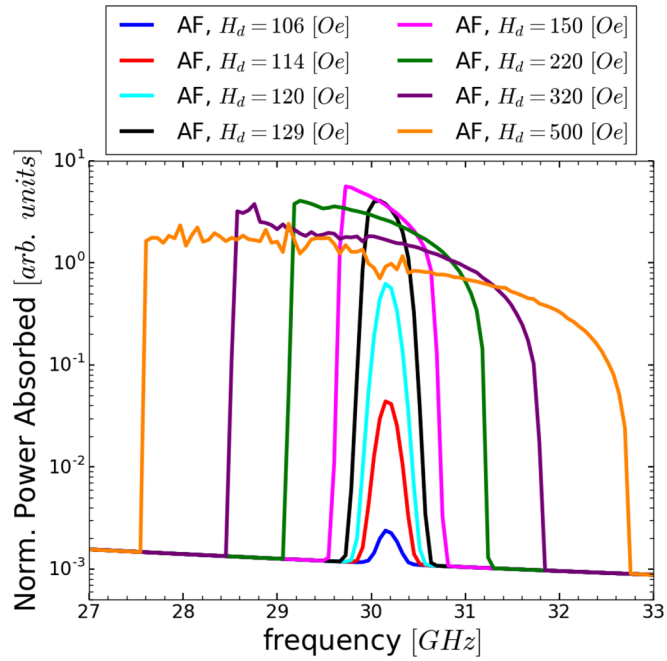

FIG. 12. Emergence and shape of the AFR response at the ($f_{\mathrm{acoustic}} + f_{\mathrm{optic}}$) mode for increasing drive amplitudes. The simulation parameters are $J_{ex} = -0.30$ erg/cm^2, $f_d \approx 30.2$ GHz, $|\gamma^A| = |\gamma^B| \approx 2.31 \times 10^5 \frac{1}{(\mathrm{A/m})\ \mathrm{s}}$ ($\approx 1.84 \times 10^7 \frac{1}{\mathrm{Oe\ s}}$), $M^A_s = M^B_s = 1.0 \times 10^6$ A/m ($4\pi M_s \approx 12.57$ kG), $d^A = d^B = 1$ nm, $\alpha^A = \alpha^B = 0.01$, $H_{\mathrm{static}} \approx 7.96 \times 10^4$ A/m (1000 Oe).

and (18), and this results in new equilibrium orientations of the magnetizations. For example, a small difference in film thicknesses (0.1–1 nm) in the numerical simulations will lead to the appearance of a small optic peak in the AF system. We note that some of these values lie outside the region where the macrospin approximation is appropriate, however it does indicate the sensitivity of the measurement to small variations in thickness. In contrast, the F system is relatively insensitive to the film thicknesses. In fact, the optic mode is only present in the F system when the magnetic properties (γ, M_s, α) of the films differ from one another. This is in contrast to the AF system where the optic mode can appear when the films have identical magnetic properties and there is only a slight difference in film thickness. (This is well known for canted systems.)

The abrupt changes in the state space configuration of a dynamic system as a parameter of the system is varied points to a bifurcation event. Probing the detailed magnetization behavior through plots of the limit cycles (attractors) and Poincaré sections near the ($f^{\mathrm{AF}}_{\mathrm{acoustic}} + f^{\mathrm{AF}}_{\mathrm{optic}}$) of Fig. 7 reveals a dramatic transition near $H_d \approx 105$ Oe from period-one motion to quasiperiodic behavior with a strong tendency to repeat its evolution every six drive periods (period-six behavior). This transition from period-one motion to quasiperiodic behavior is illustrated in Fig. 9, where we have created a bifurcation plot at the frequency of the composite mode, ($f^{\mathrm{AF}}_{\mathrm{acoustic}} + f^{\mathrm{AF}}_{\mathrm{optic}}$) ≈ 30.2 GHz. The bottom panel of Fig. 9 shows the sharp rise in AFR response at the transition from period one to quasiperiodic behavior. The quasiperiodicity occurs at drive amplitudes from roughly 105 to 300 Oe, then

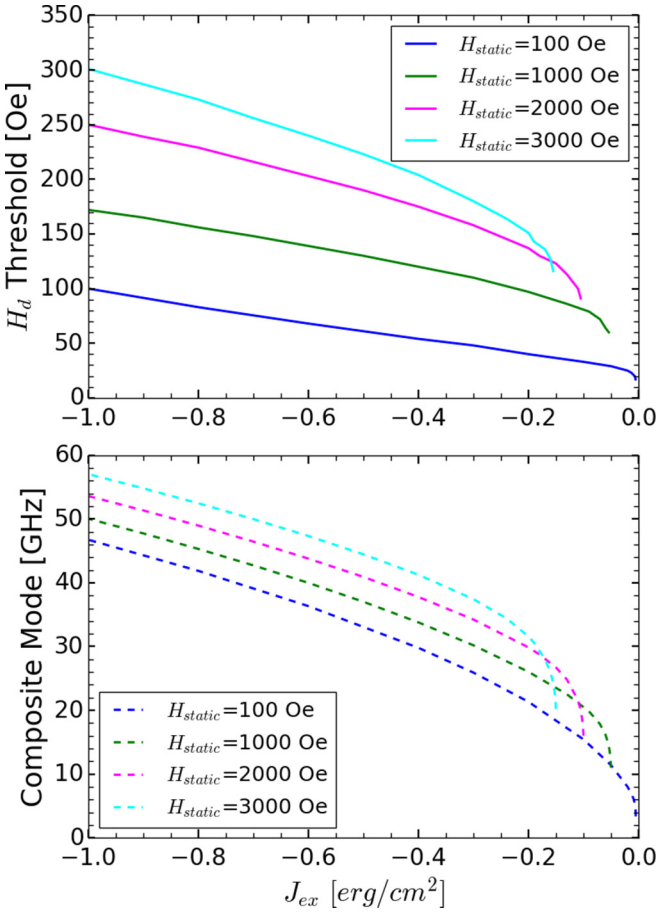

FIG. 13. Drive amplitude thresholds and composite mode frequencies as a function of both the exchange coupling and static field. $|\gamma^A| = |\gamma^B| \approx 2.31 \times 10^5$ $\frac{1}{(\mathrm{A/m})\ \mathrm{s}}$ ($\approx 1.84 \times 10^7$ $\frac{1}{\mathrm{Oe\ s}}$), $M_s^A = M_s^B = 1.0 \times 10^6$ A/m ($4\pi M_s \approx 12.57$ kG), $d^A = d^B = 1$ nm, $\alpha^A = \alpha^B = 0.01$.

the system locks on (or finds) multiperiodic attractors from 300 to 370 Oe and then begins to transition into chaotic behavior for $H_d > 370$ Oe. It is important to note here that similar bifurcation landscapes exist at the composite mode frequency for a wide variety of bilayer parameter variations, and the example presented here is illustrative of the general behavior for many other parameters (we don't show bifurcations plots of the many other configurations), though the drive amplitude of where the transitions occur for period-one→quasiperiodicity, quasiperiodicity→multiperiodic, and multiperiodic→chaos may differ.

The detailed dynamics of the magnetizations in the quasiperiodic and period-six regions of Fig. 9 are illustrated in Fig. 10. In Fig. 10(a) we plot the quasiperiodic attractor at a drive amplitude of 150 Oe, from 9.0 to 11.0 ns (60 drive periods). The motion is quasiperiodic in that the magnetization trajectories are almost repeating themselves every six drive periods. In Fig. 10(b), at $H_d = 300$ Oe the magnetization motion repeats itself every six drive periods and therefore we only plotted the trajectories over precisely six drive periods (0.2 ns) from 9.0 to 9.2 ns. It is amazing that these large amplitude complex trajectories abruptly arise from the simple small amplitude period-one motion at $H_d < 105$ Oe.

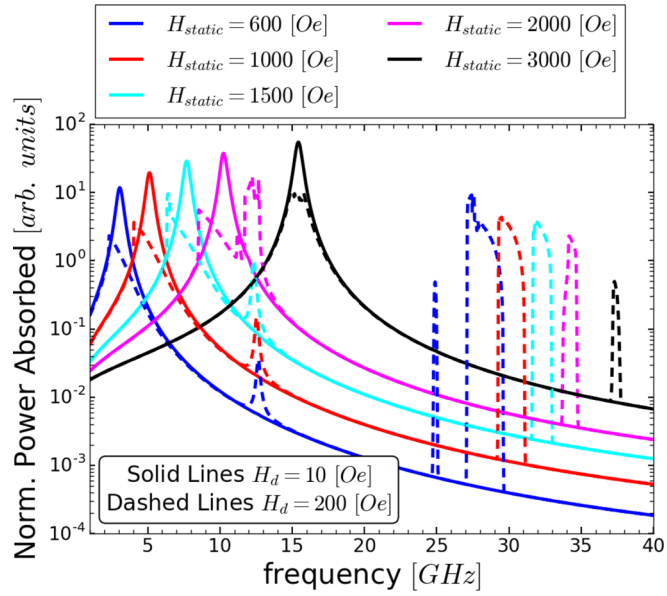

FIG. 14. Numerical AFR responses in identical films for different static field conditions. Increasing the static field shifts the acoustic mode to larger frequencies as well as the nonlinear composite mode ($f_{\mathrm{acoustic}} + f_{\mathrm{optic}}$). The simulation parameters are $J_{ex} = -0.30$ erg/cm^2, $|\gamma^A| = |\gamma^B| \approx 2.31 \times 10^5$ $\frac{1}{(\mathrm{A/m})\ \mathrm{s}}$ ($\approx 1.84 \times 10^7$ $\frac{1}{\mathrm{Oe\ s}}$), $M_s^A = M_s^B = 1.0 \times 10^6$ A/m ($4\pi M_s \approx 12.57$ kG), $d^A = d^B = 1$ nm, $\alpha^A = \alpha^B = 0.01$.

The complex behavior seen in Fig. 10 can probably be best understood by looking at the fundamental modes that comprise the composite mode behavior. The acoustic and optic mode behavior of the AF system is probably more difficult to visualize than the F system, and therefore in Fig. 11 we have plotted the late-time 3D trajectories of the fundamental modes over one drive period (the attractors of the system), so one can visually grasp the fundamental magnetization motions. When the AF coupling is strong compared to the static field strength (i.e., canting angle $\gtrsim 45^\circ$), and for a particular value of H_d, the acoustic mode has a larger amplitude motion than the optic mode and the magnetizations precess in elongated orbits like that shown in Fig. 11(a). When the system is driven at the optic mode frequency, and using the same 200 Oe value for H_d in Fig. 11(a), the optic mode magnetization amplitudes are on the order of 0.001–0.01. Due to the high-frequency small amplitude motion of the optic mode, we increased the drive amplitude in Fig. 11(b) significantly over that used for the acoustic mode, just to make it easier to visualize. (At $H_d = 200$ Oe instead of 1200 Oe, the optic mode will have a similar trajectory but with much smaller amplitude.) Now, comparing Figs. 11 and 10, one can see that the composite mode (Fig. 10) has large amplitude motion like that of the acoustic mode, and the magnetization is precessing at a frequency greater than the optic mode.

VI. TUNABILITY OF THE COMPOSITE MODE

The behavior of the strong high-frequency composite mode ($f^{\mathrm{AF}}_{\mathrm{acoustic}} + f^{\mathrm{AF}}_{\mathrm{optic}}$) introduced in the previous section can be tuned by a range of control parameters. In this section we

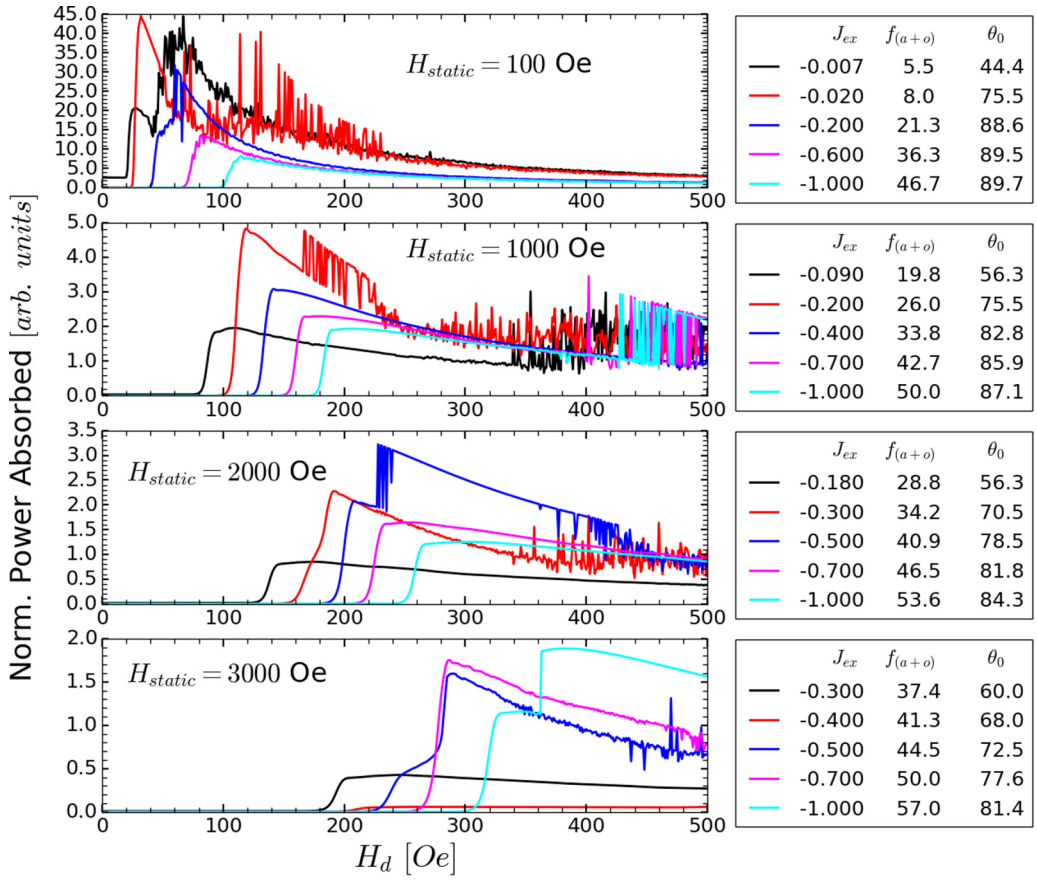

FIG. 15. Normalized power absorbed (AFR response) as a function of the drive amplitude at the acoustic plus optic mode frequency (f_{a+o}) for select exchange coupling and static field values. J_{ex} and f_{a+o} are in units of erg/cm^2 and GHz, respectively. The canting angle θ_0 is in units of degrees. $|\gamma^A| = |\gamma^B| \approx 2.31 \times 10^5 \frac{1}{(\mathrm{A/m})\ \mathrm{s}}$ ($\approx 1.84 \times 10^7 \frac{1}{\mathrm{Oe\ s}}$), $M_s^A = M_s^B = 1.0 \times 10^6$ A/m ($4\pi M_s \approx 12.57$ kG), $d^A = d^B = 1$ nm, $\alpha^A = \alpha^B = 0.01$.

present: (1) how the shape of the resonance changes with increasing drive amplitude; (2) how the frequency of the mode can be varied with different exchange coupling and static field values; (3) the effect of applying the driving microwave field along the $\hat{\boldsymbol{z}}$ direction instead of the $\hat{\boldsymbol{x}}$ direction.

We have already shown how the peak AFR response changes as a function of the drive amplitude for a fixed frequency in the bottom panel of Fig. 9, but equally important for characterization of this interesting nonlinear mode is how the width of the absorption peak changes with the drive amplitude. Figure 12 displays the emergence of the AFR response near $H_d = 106$ Oe and that it increases a few orders in magnitude from $H_d = 106 \rightarrow 129$ Oe. The maximum absorption occurs near $H_d = 150$ Oe, and the resonance band widens from a few tenths of a GHz to roughly 5 GHz over the drive amplitudes shown. It is quite interesting that the general shape of the power absorption curve remains the same even into the chaotic region at $H_d = 500$ Oe. In the analyses presented in this paper we did not calculate Lyapunov exponents to quantify the strength of the chaos. Chaos was verified by plotting Poincaré sections on unit spheres (similar to those shown in Figs. 10 and 11) over a large time interval ($100 \rightarrow 1000$ drive periods) after 10 ns of initialization and determining if the points were randomly distributed over the sphere by visual inspection.

The drive amplitude threshold for when the composite mode begins to appear is a function of both the static field and exchange coupling. This behavior is illustrated in Fig. 13 where we have plotted the H_d threshold (the onset of absorption by the composite mode) and the composite mode frequency as a function of the exchange coupling for different static fields. In general, a larger drive amplitude is needed to excite the composite mode as the static field is increased and as the strength of the exchange coupling is increased. As the exchange coupling is reduced and the magnetizations begin to align with the static field the composite mode disappears.

The frequency of the composite mode also depends on the strength of the static field and different exchange coupling values. Increasing the strength of the exchange coupling increases the torque applied to the magnetizations due to the effective exchange field $\boldsymbol{H}_{ex}^{\mathrm{A,B}} = \frac{J_{ex}}{\mu_0 d^{\mathrm{A,B}} M_s^{\mathrm{A,B}}} \frac{\boldsymbol{M}^{B,A}}{M_s^{B,A}}$. The additional torque pushes the optic mode to higher frequencies and therefore the composite mode as well.

The antiferromagnetic resonance behavior is further illustrated in Fig. 14 as the static field is increased from 600 to 3000 Oe. In this figure, one notices that increasing the static field pushes the composite mode to larger frequencies, while reducing its frequency band and peak response. (At $H_{\mathrm{static}} = 600$ Oe the nonlinearities also excited the optic mode frequency near 25.27 GHz.) Additionally, the figure tells us

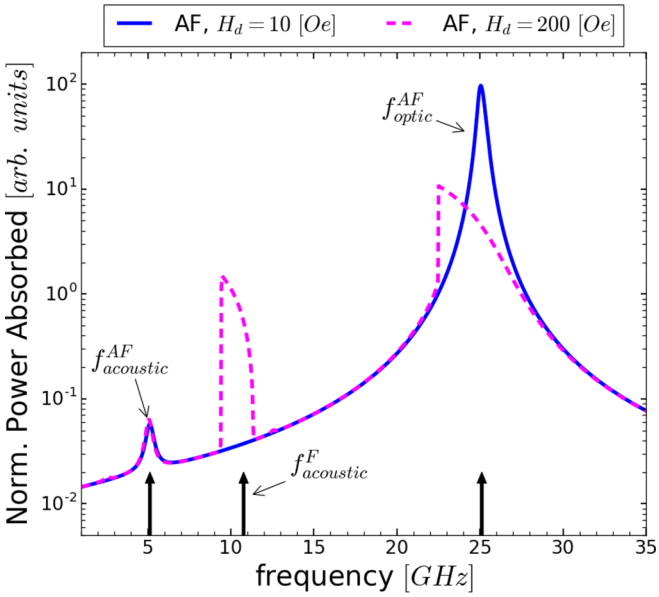

FIG. 16. Numerical AFR responses in identical films when the driving field is oriented inline with the static field. (Both fields are in the $\hat{z}$ direction.) The opticlike mode is enhanced relative to having the drive field perpendicular to the static field. In the nonlinear regime an acousticlike mode appears near that of a ferromagnetically (F) coupled system ($J_{ex} > 0$). The simulation parameters are $J_{ex} = -0.30$ erg/cm^2, $|\gamma^A| = |\gamma^B| \approx 2.31 \times 10^5 \ \frac{1}{(\mathrm{A/m})\ \mathrm{s}}$ ($\approx 1.84 \times 10^7 \ \frac{1}{\mathrm{Oe\ s}}$), $M_s^A = M_s^B = 1.0 \times 10^6$ A/m ($4\pi M_s \approx 12.57$ kG), $d^A = 1$ nm, $d^B = 0.99$ nm, $\alpha^A = \alpha^B = 0.01$, $H_{\mathrm{static}} \approx 7.96 \times 10^4$ A/m (1000 Oe).

that as the canting angles (fixed points) of the system are reduced toward the static field direction ($\hat{z}$), it takes larger drive amplitudes to excite the composite mode, in other words, the mode is easier to excite when the magnetizations of each film are further away from one another.

While the composite mode drive amplitude thresholds vary smoothly (Fig. 13) as a function of the exchange coupling and static field, the detailed characteristics of the susceptibilities as a function of the drive amplitude have a relatively complex behavior. The power absorbed as a function of the drive amplitude is presented in Fig. 15 for various exchange coupling and static fields values. Figure 15 shows a number of interesting features: (1) the peak power absorbed has a complex relationship with the exchange coupling and the drive amplitude, (2) once the power absorbed reaches a peak value it generally decreases with increasing drive amplitude, (3) as the static field is reduced the power absorbed becomes larger (with a few exceptions), and (4) the noisy regions of the curves most likely indicate regions of chaotic behavior.

Orienting the driving field along the $\hat{z}$ direction makes the optic mode easier to excite, because the mode is associated with in-phase motion in the $\hat{z}$ direction. This causes the AFR response at the optic mode frequency to be much larger than that of the acoustic mode, and therefore in Fig. 16 we see the magnitude of the responses change roles between the acoustic and optic modes compared to when the driving field is oriented perpendicular to the static field. (We added a slight asymmetry (1%) in the thicknesses of this system, so one can observe the $f^{\mathrm{AF}}_{\mathrm{acoustic}}$). Surprisingly, as the drive amplitude is increased in this AF system an acousticlike mode appears near the same frequency as that of the F system. This acousticlike mode centered about $f^{F}_{\mathrm{acoustic}}$ looks very much like that shown in Fig. 11(a) but undergoes period-two motion and not the period-one shown in the figure. The appearance of this nonlinear mode occurs near a driving field $H_d = 150$ Oe. Though not shown, as the static field is varied in this system, this nonlinear mode does indeed shift to the acoustic frequency of the F coupled system for the new static field value. Thus, when applying the driving field along the $\hat{z}$ direction of the AF system, a nonlinear mode can appear near the acoustic mode frequency of F coupled system.

VII. CONCLUSIONS

We have examined a variety of power-dependent nonlinear effects in exchange-coupled magnetic bilayers. The ferromagnetic exchange-coupled thin-film structure showed a power-dependent localization of the magnetization oscillations in one of the two films when introducing a small asymmetry in the driving field across the films. The antiferromagnetic coupled bilayer system possesses a tunable high-frequency nonlinear composite mode comprised of both the fundamental acoustic and optic modes. The absorption of this mode is strongly power dependent, with a width in absorption frequencies that is also strongly power dependent. The magnetic energy densities we explored are arguably the simplest nontrivial examples of interactions between ultrathin magnetic films which led to these interesting nonlinear phenomena. Other terms such as the surface anisotropies may be explored in future analyses. While the work presented here is theoretical and driven by a numerical analysis, it is our expectation that these effects could be measured and exploited in real devices.

[1] R. Bavli and H. Metiu, Phys. Rev. A **47**, 3299 (1993).
[2] R. Bavli and H. Metiu, Phys. Rev. Lett. **69**, 1986 (1992).
[3] R. Camley, Z. Celinski, T. Fal, A. Glushchenko, A. Hutchison, Y. Khivintsev, B. Kuanr, I. Harward, V. Veerakumar, and V. Zagorodnii, J. Magn. Magn. Mater. **321**, 2048 (2009).
[4] N. Cramer, D. Lucic, R. Camley, and Z. Celinski, J. Appl. Phys. **87**, 6911 (2000).
[5] B. K. Kuanr, Y. Khivintsev, A. Hutchison, R. Camley, and Z. Celinski, IEEE Trans. Magn. **43**, 2645 (2007).
[6] B. Heinrich and J. Cochran, Adv. Phys. **42**, 523 (1993).
[7] B. Heinrich and J. A. C. Bland (eds.), *Ultrathin Magnetic Structures II: Measurement Techniques and Novel Magnetic Properties*, Vol. 2 (Springer-Verlag, Berlin, Heidelberg, 1994).
[8] J. Cochran, J. Rudd, W. Muir, B. Heinrich, and Z. Celinski, Phys. Rev. B **42**, 508 (1990).
[9] B. Heinrich, S. Purcell, J. Dutcher, K. Urquhart, J. Cochran, and A. Arrott, Phys. Rev. B **38**, 12879 (1988).
[10] J. Cochran and J. Dutcher, J. Appl. Phys. **64**, 6092 (1988).

[11] Z. Celinski, K. Urquhart, and B. Heinrich, J. Magn. Magn. Mater. **166**, 6 (1997).

[12] S. Li, C. Wang, X.-M. Chu, G.-X. Miao, Q. Xue, W. Zou, M. Liu, J. Xu, Q. Li, Y. Dai *et al.*, Sci. Rep. **6**, 33349 (2016).

[13] J. Lindner and K. Baberschke, J. Phys.: Condens. Matter **15**, S465 (2003).

[14] C. Bilzer, T. Devolder, P. Crozat, C. Chappert, S. Cardoso, and P. Freitas, J. Appl. Phys. **101**, 074505 (2007).

[15] A. Konovalenko, E. Lindgren, S. Cherepov, V. Korenivski, and D. Worledge, Phys. Rev. B **80**, 144425 (2009).

[16] L. H. Bennett and R. E. Watson, *Magnetic Multilayers* (World Scientific, Singapore, 1994).

[17] M. Romera, B. Lacoste, U. Ebels, and L. Buda-Prejbeanu, Phys. Rev. B **94**, 094432 (2016).

[18] D. Gusakova, D. Houssameddine, U. Ebels, B. Dieny, L. Buda-Prejbeanu, M. Cyrille, and B. Delaët, Phys. Rev. B **79**, 104406 (2009).

[19] A. Jenkins, B. Lacoste, G. Geranton, D. Gusakova, B. Dieny, U. Ebels, and L. Buda-Prejbeanu, J. Appl. Phys. **115**, 083911 (2014).

[20] S. Rezende and F. De Aguiar, Phys. Lett. A **208**, 286 (1995).

[21] I. D. Mayergoyz, G. Bertotti, and C. Serpico, *Nonlinear Magnetization Dynamics in Nanosystems* (Elsevier, Amsterdam, 2009).

[22] P. E. Wigen, *Nonlinear Phenomena and Chaos in Magnetic Materials* (World Scientific, Singapore, 1994).

[23] L. F. Alvarez, O. Pla, and O. Chubykalo, Phys. Rev. B **61**, 11613 (2000).

[24] Y. Khivintsev, J. Marsh, V. Zagorodnii, I. Harward, J. Lovejoy, P. Krivosik, R. Camley, and Z. Celinski, Appl. Phys. Lett. **98**, 042505 (2011).

[25] Y. Khivintsev, B. Kuanr, T. Fal, M. Haftel, R. Camley, Z. Celinski, and D. Mills, Phys. Rev. B **81**, 054436 (2010).

[26] M. Phelps, K. Livesey, A. Ferona, and R. Camley, Europhys. Lett. **109**, 37007 (2015).

[27] R. K. Smith, M. Grabowski, and R. Camley, J. Magn. Magn. Mater. **322**, 2127 (2010).

[28] R. K. Smith, M. Grabowski, and R. Camley, J. Magn. Magn. Mater. **321**, 3472 (2009).

[29] D. Laroze, P. Vargas, C. Cortes, and G. Gutierrez, J. Magn. Magn. Mater. **320**, 1440 (2008).

[30] J. Bragard, H. Pleiner, O. Suarez, P. Vargas, J. Gallas, and D. Laroze, Phys. Rev. E **84**, 037202 (2011).

[31] J. C. Slonczewski, J. Magn. Magn. Mater. **159**, L1 (1996).

[32] A. M. Ferona and R. E. Camley, Phys. Rev. B **95**, 104421 (2017).

[33] S. Li, Q. Xue, J.-G. Duh, H. Du, J. Xu, Y. Wan, Q. Li, and Y. Lü, Sci. Rep. **4**, 7393 (2014).

[34] D. Worledge, Appl. Phys. Lett. **84**, 2847 (2004).

[35] D. Wei, *Micromagnetics and Recording Materials* (Springer Science and Business Media, Heidelberg, New York, 2012).

[36] T. L. Gilbert, IEEE Trans. Magn. **40**, 3443 (2004).

[37] M. Urbaniak, T. Luciński, and F. Stobiecki, J. Magn. Magn. Mater. **190**, 187 (1998).

[38] Y. Kozono, M. Komuro, S. Narishige, M. Hanazono, and Y. Sugita, J. Appl. Phys. **61**, 4311 (1987).

[39] E. Hairer, S. P. Norsett, and G. Wanner, *Solving Ordinary Differential Equations I. Nonstiff Problems*, 2nd ed. (Springer-Verlag, Berlin, Heidelberg, 1993).

[40] A. C. Hindmarsh, IMACS Transactions on Scientific Computation **1**, 55 (1983).

[41] M. d'Aquino, C. Serpico, and G. Miano, J. Comput. Phys. **209**, 730 (2005).

[42] J. Smith and H. G. Beljers, Philips Res. Rep. **10**, 113 (1955).

[43] M. Kuteifan, M. Lubarda, S. Fu, R. Chang, M. Escobar, S. Mangin, E. Fullerton, and V. Lomakin, AIP Advances **6**, 045103 (2016).

[44] M. Balanda, Acta Phys. Pol. A **124**, 964 (2013).

[45] D. Martien, *Introduction to AC Susceptibility* (Quantum Design, San Diego, CA, 1994).